Review

Effect of Precursor Powder on the Solidification Microstructure and Superconducting Properties of Ceramic Superconducting Materials: A Review

Zhenguo Zhang , Minghui Tang * , Hao Zhou , Wei Ren , Shuhua Yang * , Dongliang Wang * , Yanwei Ma

Posted Date: 17 March 2026

doi: 10.20944/preprints202603.1268.v1

Keywords: precursor powder modification; solidification process; superconducting property; microstructural control

 doi:10.20944/preprints202603.1268.v1

Review

Effect of Precursor Powder on the Solidification Microstructure and Superconducting Properties of Ceramic Superconducting Materials: A Review

Zhenguo Zhang [1,2], Minghui Tang [3,*], Hao Zhou [1,2], Wei Ren [3], Shuhua Yang [1,*], Dongliang Wang [2,3,4,*] and Yanwei Ma [2,3,4]

[1] School of Material Science and Engineering, University of Jinan, Jinan 250022, China
[2] Shandong Key Laboratory of Advanced Electromagnetic Conversion Technology, Institute of Electrical Engineering and Advanced Electromagnetic Drive Technology, Qilu Zhongke, Jinan, 250013, China
[3] Beijing Key Laboratory of Applied Superconductivity, Institute of Electrical Engineering, Chinese Academy of Sciences, Beijing, 100190, China
[4] University of Chinese Academy of Sciences, Beijing 100049, China
* Correspondence: tangminghui@mail.iee.ac.cn (M.T.); yangshuhua78@163.com (S.Y.); dongliangwang@mail.iee.ac.cn (D.W.)

Abstract

The solidification process is crucial for preparing high-performance ceramic superconductor. The solidification process is strongly dependent on the characteristics of the starting powder, including particle size, morphology, and phase purity. This review concisely examines the study on four key ceramic superconductors: REBCO, Bi-2212, FeSeTe, and MgB_2. In REBCO, additives such as CeO_2, Pt, or BaO_2 powder can refine the RE-211 phase. In Bi-2212, Pb or Nb powder additions stabilize the high-T_c phase. For FeSeTe, doping with F or Co modifies phase separation and introduces $\Delta\kappa$ pinning. Meanwhile, in MgB_2, the incorporation of SiC nanoparticles powder generates effective pinning centers. Concurrently, processing conditions exert a decisive influence on the final microstructure, as demonstrated by the TSMG/TSIG route in REBCO, partial melting parameters for Bi-2212, specific cooling protocols and thermal treatments for FeSeTe, and optimized sintering and post-annealing processes for MgB_2. Future research directions should prioritize fundamental understanding of phase separation mechanisms during powder processing, development of multi-component doping strategies for powder modification, and advancement of scalable powder processing routes for practical conductor architectures.

Keywords: precursor powder modification; solidification process; superconducting property; microstructural control

1. Introduction

The promising prospects of practical superconducting materials for high-power applications are constrained by a common and critical issue. The solidification process is a main process crucial for preparing high-performance bulk and round wire. the prevalent occurrence of phase separation during solidification and heat treatment processes. This microstructural heterogeneity manifests in varied forms across different material systems, yet consistently leads to the degradation of macroscopic performance.

In the REBCO melt textured bulk materials, the complex multi-element reactions and non-equilibrium solidification readily induce texture imperfections, inhomogeneous distribution of flux pinning centers, and segregation of RE-211 phases, significantly compromising the current carrying capacity under high magnetic fields and the uniformity of properties [1–4]. Similarly, in the isotropic bismuth-based Bi-2212 materials, incomplete phase transformation and porosity during melt

 doi:10.20944/preprints202603.1268.v1

processing not only reduce the critical current density (J_c) but also pose serious challenges to their stability in very high-field magnet applications [5–7]. For iron-based Fe(Se, Te) superconductors and the intermetallic compound MgB_2, phase separation primarily manifests as compositional fluctuations (e.g., Se/Te) or deviation from stoichiometry of key elements (e.g., Mg), subsequently triggering secondary phase precipitation, weak intergranular coupling, and pore formation, which directly impair electrical connectivity and flux pinning effectiveness [8-12]. Therefore, despite the diversity of material systems, microstruct [8–12ural instability and chemical inhomogeneity resulting from solidification induced phase separation have emerged as a fundamental bottleneck limiting the enhancement of J_c, reproducibility of performance, and high-field applicability across various practical superconducting materials [13].

Beyond the common issue of phase separation, a unifying feature across these superconductor families is identified. Their entire processing chain is initiated from precursor powders. This includes oxide mixtures for REBCO, Bi-2212 precursor powder, elemental Fe, Se, and Te blends for iron-based superconductors, and Mg and B mixtures for MgB_2. The initial characteristics of these powders, such as particle size distribution, phase purity, and dopant homogeneity, are not considered incidental. Instead, they are regarded as critical boundary conditions that govern the thermodynamic and kinetic pathways of all subsequent transformations. Therefore, a profound understanding of powder precursors is established as the primary foundation for dictating the final microstructure and, consequently, the ultimate superconducting performance.

All are processed from functional powder precursors. Whether it is the RE-123 and RE-211 powders for melt-textured REBCO [14], the Bi-2212 powder packed into silver tubes for round wires [5], the elemental Fe, Se, and Te powders for iron-based superconductors [9,15], or the Mg and B powders for in-situ MgB_2 synthesis [16,17], the journey to a high-performance superconductor is invariably begun with a powder. The initial characteristics of these powders, including particle size distribution, phase purity, morphology, agglomeration state, and the homogeneity of any dopant distribution, are considered not merely incidental details. Instead, they are regarded as critical boundary conditions that govern the thermodynamic and kinetic pathways of subsequent solidification and phase separation.

Consequently, a profound comprehension and precise control of phase separation during solidification is pivotal for transitioning practical superconducting materials from laboratory research to engineering applications. This review systematically examines the effect of precursor powder on the solidification microstructure and superconducting properties of ceramic superconducting materials. It assesses the consequent effects on critical superconducting properties, including J_c, the transition temperature (T_c), and microstructural connectivity. Furthermore, the primary strategies for controlling this phenomenon are summarized. The objective is to provide a theoretical foundation and directional guidance for the process optimization and performance enhancement of these materials.

2. Influence of Precursor Powder Characteristics on the Solidification Process and Performance of High-T_c Cuprate Superconductors

2.1. REBCO

In the fabrication process of REBCO bulk superconductors, the treatment of precursor powders represents the logical starting point that fundamentally determines the final sample performance, with a clear causal chain linking powder purity, particle size, distribution, final phase assemblage, flux pinning characteristics, and current carrying capacity. The chemical purity and phase composition of precursor powders form the basis for ensuring the final phase purity of the samples. If high purity precursor powders are not obtained at the initial synthesis stage, subsequent heat treatments cannot eliminate impurity phases, which ultimately compromises the superconducting properties. For instance, in the preparation of Y_2BaCuO_5 powder by Antončík et al. [18], high purity raw materials (99.99% Y_2O_3 and CuO) were employed, and repeated grinding and calcination were

 doi:10.20944/preprints202603.1268.v1

conducted between 1138 K and 1173 K. X ray diffraction analysis subsequently confirmed that a high purity sample without detectable impurity phases was obtained, which established the foundation for accurate measurement of its thermodynamic properties. Figure 1 presents the microstructural morphology and elemental distribution analysis of the Y-211 powder from that study. As can be observed in the figure, the prepared Y-211 powder particles exhibited uniform dimensions, primarily distributed in the range of 1 to 5 μm. Furthermore, energy dispersive spectroscopy elemental mapping confirmed that Y, Ba, Cu, and O elements were uniformly distributed throughout the particles without any compositional segregation, which directly demonstrates the high purity and chemical homogeneity of the powder [18].

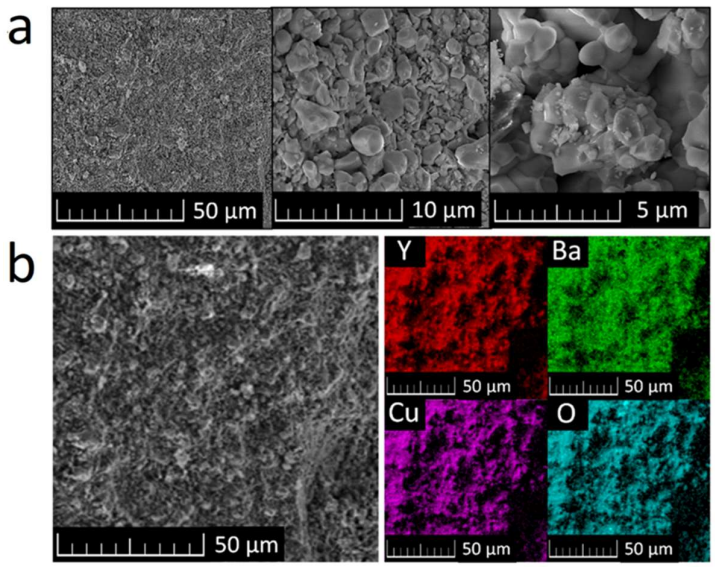

Figure 1. Morphology of the Y_2BaCuO_5 particles observed by SEM (a) and the associated elemental mappings acquired via EDS (b). Adapted from [18] with permission.

Once purity has been ensured, particle size becomes the most critical controllable variable. Extensive comparative studies have confirmed that refining the precursor powder particle size represents the most effective means of controlling the dimensions of the non superconducting RE-211 second phase particles in the final microstructure. This process follows the principle of particle size inheritance: finer precursor powders result in smaller RE-211 particles retained within the RE-123 matrix, thereby introducing more pinning interfaces within the superconductor. For example, when ultra fine Gd-211 powder with an average particle size of only 0.1 μm was employed, submicron sized Gd-211 particle distributions were obtained in Gd-Ba-Cu-O bulk materials, which significantly enhanced J_c [19]. Additionally, when the infiltration growth process is adopted, powder treatment directly influences the uniformity of liquid phase infiltration and subsequent reactions, which consequently determines the distribution homogeneity of RE-211 particles in the final samples. This approach avoids the second phase free regions commonly observed in conventional melt textured samples, resulting in more uniform and denser microstructures [14,20].

However, powder refinement is not simply a matter of achieving the smallest possible particle size; it must be matched with the growth kinetics. In the top seeded melt growth process, excessively fine Y-211 powder tends to be pushed by the growth front rather than trapped near the seed crystal, which leads to the formation of macroscopic regions devoid of pinning centers beneath the seed and adversely affects the uniformity of performance [19]. In the infiltration growth process, by adjusting the cooling time, the Ostwald ripening of Y-211 particles can be effectively controlled, thereby avoiding particle coarsening that would otherwise occur with excessively long processing times and maintaining a uniform microstructure [21].

 doi:10.20944/preprints202603.1268.v1

Driven by their broad transformative potential, high-temperature superconductor (HTS) research constitutes a key research direction in materials science [4,22]. With their superior performance and enhanced efficiency, second-generation high-temperature superconductors (2G-HTS) hold great promise for critical applications ranging from energy transmission and medical imaging to advanced scientific instrumentation [1,23,24]. Since their discovery in 1986, REBCO (RE = rare earth element) high temperature superconducting bulks has attracted extensive attention due to their outstanding flux [24] trapping performance (>5 T) at liquid nitrogen temperature (77 K) [25]. The superconducting properties, particularly J_c and trapped field, are fundamentally dictated by the microstructural features developed during the solidification process. Single-grain REBCO bulk superconductors are typically fabricated via melt processes such as Top-Seeded Melt-Growth (TSMG) or Top-Seeded Infiltration and Growth (TSIG) [14,20,26]. Both methods are based on a peritectic reaction, wherein the $REBa_2Cu_3O_{7-\delta}$ (RE-123) phase decomposes incongruently upon heating into solid RE_2BaCuO_5 (RE-211) particles and a Ba-Cu-O liquid phase. The subsequent slow cooling stage facilitates a seeded peritectic reaction between the RE-211 phase and the liquid phase [14,19]. This process results in the formation of a textured RE-123 single grain, thereby incorporating unreacted RE-211 particles, pores, and other non-superconducting phases as inclusions.

Phase separation is a critical and ubiquitous phenomenon during the solidification of REBCO superconductors, primarily manifested by the formation and distribution of non-superconducting secondary phases within the RE-123 matrix. The scale and morphology of these phase separated structures can be effectively governed through precise design of the sample composition and solidification pathway. This complex solidification process inherently leads to phase separation with varying degrees of refinement. The morphology, size, and distribution of these separated phases, which are governed by the processing conditions directly determine the final properties of the material.

This chapter will systematically review the phase separation phenomena in REBCO materials during solidification. It will focus on two primary control strategies: compositional modification and process optimization, and will elaborate on how these microstructural features influence superconducting performance.

2.1.1. Compositional Design of Precursor Powders for Phase Refinement

The introduction of specific additives or the precise modification of the precursor composition represents one of the most direct and effective strategies for controlling the phase separation of the RE-211 secondary phase.

In the conventional TSMG process, the precursor powder typically consists of RE-123 mixed with an excess of RE-211, a common nominal ratio being 75:25 wt% [26]. The incorporation of the RE-211 phase serves multiple critical purposes: (i) to supply a sufficient source of RE elements for the peritectic growth of the RE-123 matrix, thereby promoting rapid crystal growth, (ii) to minimize the loss of the liquid phase during the high-temperature melting stage by reducing its mobility, and (iii) ultimately, to yield a dispersion of fine, non-superconducting RE-211 particles within the RE-123 matrix after solidification, which act as effective flux-pinning centers [27,28].

Other rare earth systems, such as GdBCO and SmBCO, exhibit higher T_c and J_c compared to YBCO. However, due to the similar atomic radii of rare earth and Ba atoms, these systems are prone to the formation of $RE_{1+x}Ba_{2-x}Cu_3O_y$ solid solutions, which significantly degrade their superconducting properties [29]. To visually demonstrate the remarkable effect of compositional design on regulating the superconducting properties of REBCO, Table 1 [30–35] summarizes the achieved critical current densities via the addition of various secondary phases.

 doi:10.20944/preprints202603.1268.v1

Table 1. J_c of REBCO bulks at 77 K under self-field for various doping conditions [30–35].

Bulk Sample	Doping Condition	J_c at 77 K, self-field (A/cm²)	
GdBCO	70 wt% Gd123 + 30 wt% Gd211 +1 wt% BaO_2+ 0.1 wt% Pt	7.4×10^4	[31]
GdBCO	Gd123 : Gd211 : BaO_2 = 1:0.4:0.1 + 10 wt% Ag_2O + 0.5 wt% Pt	8.6×10^4	[30]
GdBCO	7 wt% YGdNb-11411 + 1 wt% CeO_2	8.64×10^4	[35]
SmBCO	75 wt% Sm123 + 25 wt% Sm211 +2 wt% BaO_2+ 1 wt% CeO_2	4×10^4	[33]
YBCO	70 wt% Y123 + 30 wt% Y211 + 2 wt% CeO_2	5.7×10^4	[32]
YBCO	Y123:Y_2O_3 = 1:0.3 + 2 wt% CeO_2	5.2×10^4	[34]

Studies indicate that the addition of BaO_2 at concentrations of 1-10 wt% in GdBCO is an effective strategy for suppressing solid solution formation [1,30,31,36,37], thereby facilitating the production of bulk samples with enhanced superconducting properties. During the melt growth process, BaO_2 serves as an additional source of both oxygen and barium, suppressing the formation of Ba-Cu-O impurities and reducing the occurrence of non-stoichiometric solid solutions caused by barium deficiency, thereby promoting the formation of pure phase RE-123 [35]. Furthermore, the addition of approximately CeO_2 [32,33], Pt [34,38], $YGdBa_4CuNbO_y$ [35] effectively suppresses the Ostwald ripening of RE_2BaCuO_5 (RE-211) particles during melt growth. This results in a refined and uniform distribution of RE-211 particles within the superconducting matrix. Besides, researchers have found that introducing second-phase additives can create a higher density of flux-pinning centers within the RE-123 matrix. A prime example is the YGdNb-11411 nanoparticle, which, due to its high chemical stability and non-reactivity with the RE-123 phase, acts as an effective pinning center without inducing solid solutions or deleterious secondary phases [39–41].

Figure 2 directly compares the performance of the REBCO samples listed in Table 1, highlighting a crucial distinction in how different compositional modifications affect the superconductor. The key insight from this comparison is that while the addition of chemical additives (e.g., BaO_2, Pt, CeO_2) effectively enhances the self-field J_c, it often results in a strong magnetic field dependence, leading to a rapid decline at higher fields. This is evident in the similar, steeper degradation curves of samples like GdBCO (BaO_2+Pt) [31] and YBCO (CeO_2) [32]. In contrast, introducing designed secondary phase nanoparticles (e.g., YGdNb-11411) serves a different primary function: to directly and robustly enhance flux-pinning capability. The GdBCO sample with YGdNb-11411 nanoparticles demonstrates this principle clearly. It not only achieves the highest self-field J_c but, more importantly, exhibits the most gradual decay with increasing field. This superior performance across the entire 0-5 T range signifies the creation of a more effective pinning. Therefore, this figure underscores a strategic guideline for performance optimization: additives are essential for refining the primary microstructure and boosting zero-field performance, but the incorporation of tailored secondary phase nanoparticles is critical for building strong, field-independent pinning centers that ensure high current capacity under practical magnetic operating conditions.

 doi:10.20944/preprints202603.1268.v1

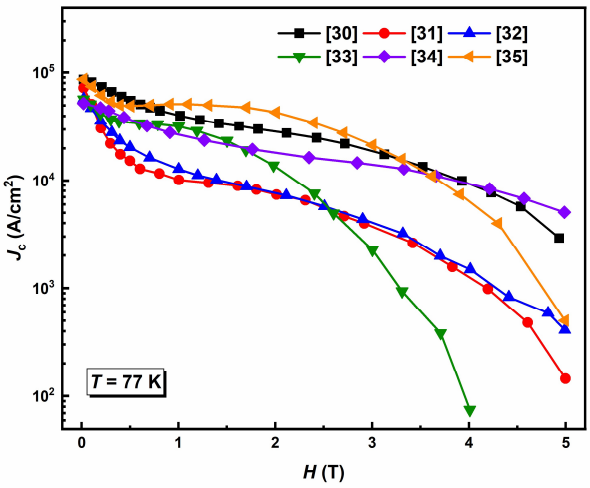

Figure 2. Magnetic field dependence of the J_c at 77 K for the doped REBCO bulk superconductors listed in Table 1.

2.1.2. Processing Solidified Microstructures from Engineered Powders

The solidification pathway plays a critical role in determining the spatial distribution of the RE-211 phase in REBCO, influencing its phase separation at both the macro- and micro-scale. Figures 3a and b show that the growth of the RE-123 phase exhibits a strong anisotropy between its a-b plane and c-axis, which consequently determines the final distribution and dimensions of RE-211 inclusions within the single-domain matrix [42].

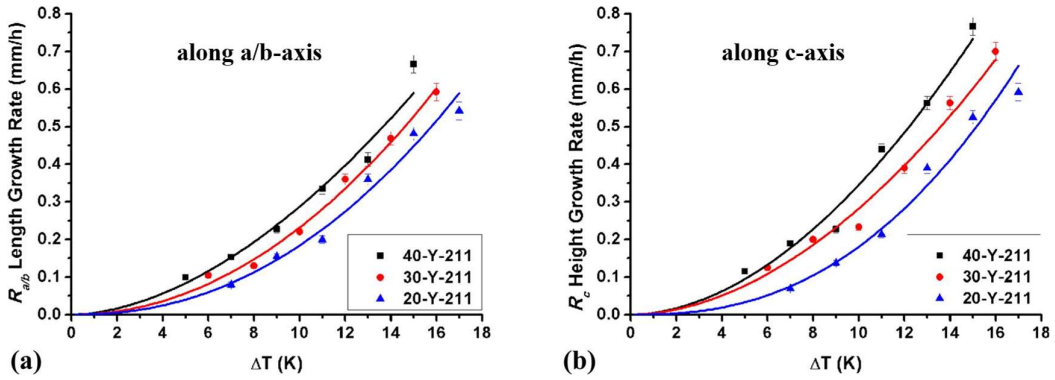

Figure 3. Growth rates of YBCO as a function of undercooling temperature (ΔT): (a) along the a/b-axis and (b) along the c-axis, for samples with varying Y-211 content (20, 30, and 40 wt%). Reprinted with permission from [42]. Licensed under CC BY 4.0.

The growth velocity of the RE-123 phase and the grain size of the RE-211 particles determine whether the RE-211 particles are trapped within the matrix or is pushed by the advancing growth front [43]. A larger undercooling promotes a higher growth rate, which favors the trapping of finer particles, leading to a uniform distribution of refined RE-211. In contrast, a smaller undercooling can result in particle pushing, causing macroscopic segregation [3,42]. In the TSMG process, the final distribution of RE-211 particles and the formation of microstructural defects in REBCO bulks are collectively determined by the growth mode (isothermal or undercooling) and the characteristics of the precursor powder. An optimized isothermal growth process utilizing a specifically formulated precursor powder has been shown to yield a superior spatial distribution of refined RE-211 inclusions [44].

Table 2 [14,20,45] shows a comparative summary of the TSMG and TSIG processes for REBCO bulk superconductors, detailing precursor materials, in-situ reactions, and the results. In the TSIG

 doi:10.20944/preprints202603.1268.v1

process, the liquid phase source is comprised of a mixture of Y_2O_3, CuO, and $BaCuO_2$ in a specific molar ratio.

Table 2. Comparison of the TSMG and TSIG Processing Techniques [14,20,45].

‘	TSMG	TSIG
Raw material	RE-123 + RE-211	Liquid + RE-211
Reaction	RE-123→RE-211+Ba-Cu-O+CuO $CuO \rightarrow Cu_2O+\frac{1}{2}O_2 \uparrow$ RE-211+Ba-Cu-O+CuO→RE-123	RE-211+Ba-Cu-O+CuO→RE-123
Result	Formation of Pores RE-211 Particles Agglomeration RE-211 Particles Coarsening	Homogeneous distribution of RE-211 Particles

A comparative analysis of the two processing techniques reveals that the TSIG route is fundamentally superior for microstructural control [14,20,46,47]. In the conventional TSMG process, the peritectic decomposition of the RE-123 phase generates gaseous species (leading to pore formation) and concurrently precipitates RE-211 particles. These newly formed RE-211 particles are highly susceptible to coarsening via Ostwald ripening within the liquid matrix and become heterogeneously distributed due to liquid phase migration. Consequently, this results in a microstructure characterized by coarse and inhomogeneous RE-211 inclusions, as visually contrasted in Figures 4a and b. In contrast, the TSIG technique entirely circumvent the peritectic decomposition of the RE-123 phase. This process utilizes a pre-sintered preform of fine, precursor RE-211 powder as a stationary solid skeleton, which is infiltrated by a liquid phase source. Since the RE-211 particles are immobilized within this rigid framework, their coarsening is effectively suppressed, and their initial fine size and uniform spatial distribution are preserved throughout the growth process. This yields the refined, dense, and homogeneous dispersion of RE-211 particles evident in Figures 4c and d.

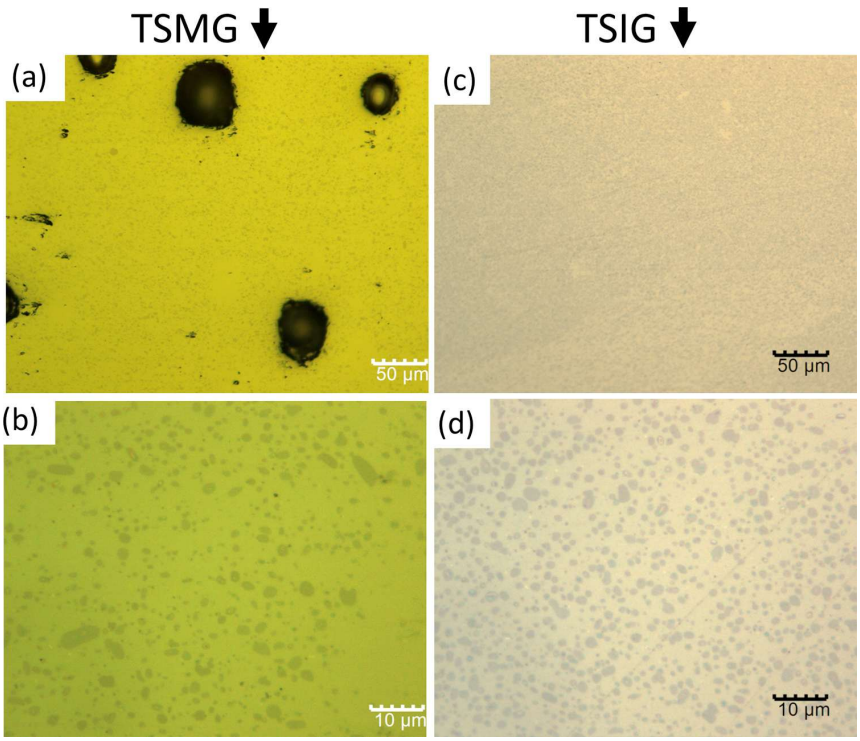

Figure 4. Optical micrographs of YBCO samples fabricated by (a, b) the Top-Seeded Melt Growth process and (c, d) the Top-Seeded Infiltration and Growth process. (b) and (d) are higher-magnification views of the regions outlined in (a) and (c), respectively [20] (CC BY 4.0).

 doi:10.20944/preprints202603.1268.v1

The superior microstructural homogeneity achieved by TSIG is also reflected in the uniformity of the superconducting properties [14]. Figure 5 compares the magnetic field dependence of J_c at 77 K for YBCO bulk samples fabricated via TSMG and TSIG routes, with multiple data points representing different sampling locations within the same bulk. The TSMG processed samples exhibit higher peak J_c values but show significant positional variation, indicative of microstructural heterogeneity such as uneven RE-211 distribution and porosity. In contrast, TSIG processed samples display lower but remarkably consistent J_c values across all measured positions, demonstrating the improved microstructural uniformity imparted by the TSIG process.

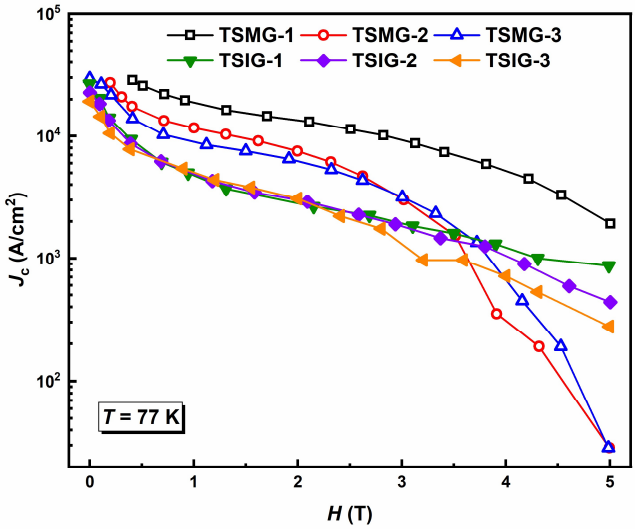

Figure 5. Magnetic field dependence of J_c at 77 K for YBCO bulk superconductors fabricated by TSMG and TSIG processes. The suffixes "-1", "-2", and "-3" denote measurements taken from different locations within the same bulk sample. Data are extracted from [14] (CC BY 3.0).

Additionally, the content and distribution of RE-211 inclusions in the RE-123 matrix can be optimized by adjusting key processing parameters, specifically, infiltration temperature, time, and liquid phase content in the precursor [20,45]. This approach effectively addresses the issue of excessive RE-211 (> 40%) that impaired the performance of early TSIG samples [14]. The development of the two-step BA-TSIG process, which separates the infiltration and grain growth stages, has led to a significant improvement in the precision of phase separation control and the overall reliability of the process [48]. The fabrication of REBCO bulk superconductors inherently relies on the quality of precursor powders. In practice, RE-123 and RE-211 powders are most commonly prepared by solid-state reaction. The particle size, purity, and stoichiometry of these starting powders are known to have a direct impact on the subsequent melt growth process. The critical role of precursor characteristics is further exemplified in Figure 6, which contrasts the outcomes of using coarse versus fine Y-211 powders [27]. The finer Toshima powder (Figures 6b and d) not only promotes a larger single-grain growth area but also yields a microstructure with markedly refined and homogeneously dispersed Y-211 particles, compared to the coarser Nexans powder (Figures 6a and c). This visual evidence underscores that controlling the initial state of the phase-separating component (Y-211) is as crucial as optimizing the thermal process parameters for achieving desirable pinning architectures.

 doi:10.20944/preprints202603.1268.v1

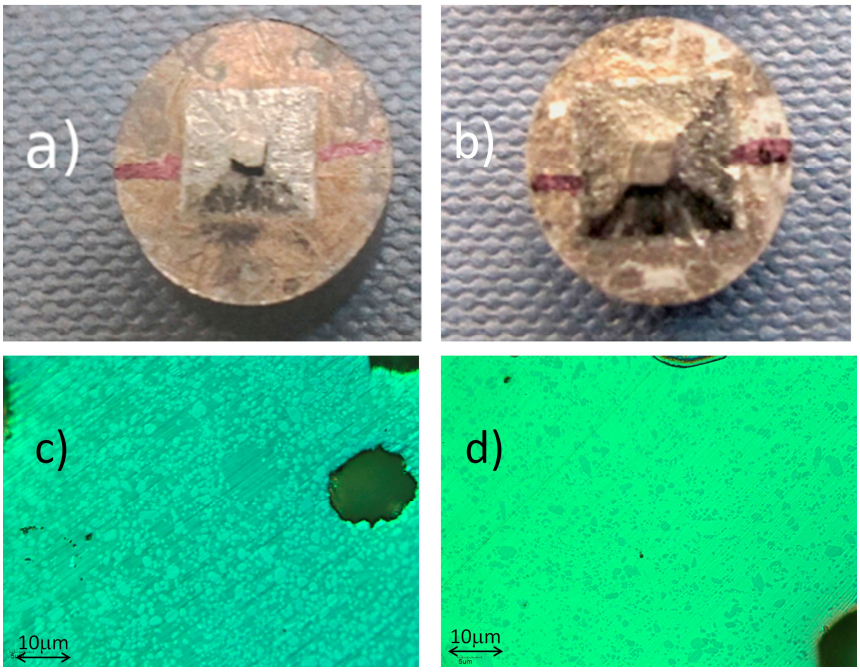

Figure 6. Influence of Y-211 precursor powder size on single-grain growth morphology and final microstructure. (a, b) Top surface view and (c, d) corresponding optical micrographs of YBCO single grains fabricated from coarse Nexans Y-211 powder (a, c) and fine Toshima Y-211 powder (b, d). Image from [27] under the terms of the CC BY 3.0.

The final properties of REBCO superconductors are critically determined by the identity, scale, and uniformity of the phase distribution resulting from phase separation. RE-211 particles serve as the primary natural pinning centers in REBCO superconductors. Their pinning mechanism originates primarily from defects such as dislocations and stacking faults, which are generated at the RE-211/RE-123 interface due to lattice mismatch [49,50]. Consequently, the optimization of RE-211 particle size and distribution represent a key approach to increasing the effective pinning site density [18], thereby improving critical current performance. For instance, the J_c of RE-Ba-Cu-O bulk superconductors can be markedly improved by refining the RE_2BaCuO_5 (RE211) phase through several methods, including the optimization of solidification conditions [21,45,51], the addition of the second phases [29,35,52,53] (such as, CeO_2, Pt, and $Y_2Ba_4CuNbO_y$).

However, in REBCO superconductors, the formation of a solid solution is detrimental, as it disrupts phase homogeneity, resulting in a severe degradation of both T_c and J_c [35,45]. Besides, an inhomogeneous macroscopic distribution of the RE-211 phase can lead to uneven current transport paths and the formation of local weak links, which consequently degrades the overall trapped field performance [54–57]. In response to these challenges, a range of integrated strategies has been developed to further optimize the growth uniformity of single-domain REBCO. These strategies include the optimization of seeded growth techniques, precise control over the composition and distribution of the RE-211 phase in precursor powders, and the implementation of buffer layers [1,14,20,45]. Complementing the compositional and process engineering approaches discussed above, these methods are designed to suppress macro-segregation and structural defects on a larger scale. Collectively, they provide a more comprehensive technological pathway for achieving reliable fabrication of high-performance REBCO superconductors.

2.2. Bi-2212

The properties of precursor powders and their processing conditions are critical factors that determine the final performance, particularly the J_c, of Bi-2212 superconducting wires and coils. The

 doi:10.20944/preprints202603.1268.v1

stoichiometry and phase assemblage of the powder fundamentally control the reaction pathway during subsequent heat treatments. While precursor powders with a nominal "521" composition ($Bi_{2.17}Sr_{1.94}Ca_{0.89}Cu_2O_x$) are widely utilized, the fabrication route, whether co-precipitation or spray combustion, can lead to significant differences in phase purity and distribution, which directly impacts the wire performance [58,59]. The uniformity of the calcination process is largely governed by powder packing and heating protocols. It has been demonstrated that high heating rates or densely packed powders can trap CO_2 released during carbonate decomposition. This entrapment creates a locally reduced oxygen partial pressure, which lowers the melting point of Bi-oxide phases and induces premature melting at temperatures as low as 740 ℃. Such melting is detrimental as it promotes phase separation, grain coarsening, and overall precursor inhomogeneity, ultimately degrading J_c [60]. To preserve homogeneity and avoid the formation of this transient melt, a loosely packed powder bed combined with moderate heating rates is required to ensure adequate gas exchange.

Furthermore, the calcination temperature itself dictates the phase assemblage and morphology of the precursor powder. Low-temperature calcination (e.g., 710 ℃) yields a homogeneous mixture of fine, intermediate phases. These phases are considered favorable as they lead to a more uniform peritectic decomposition during the final partial melt processing, thereby supporting a high J_c. In contrast, high-temperature calcination promotes the formation of large, plate-like grains (such as the 2201 phase), which contribute to compositional inhomogeneity on a larger scale and are correlated with reduced current-carrying capacity [60].

Bi-2212, as a representative high-temperature superconducting cuprate, is a promising candidate for high-field magnet applications due to its excellent processability, such as the ease of fabricating isotropic round wires, and its potential for high J_c under high magnetic fields. However, similar to many complex oxides, Bi-2212 is highly susceptible to phase separation during solidification from the high-temperature melt or subsequent heat treatment, resulting in a complex microstructure that influences its superconducting properties. This section systematically discusses the control of phase separation in Bi-2212 and its correlation with performance from two perspectives: compositional doping and processing techniques.

2.2.1. Powder Doping Strategies for Microstructural Optimization

In the Bi-2212 system, elemental doping serves as an important means to regulate phase separation behavior during solidification and ultimately tailor the superconducting properties. The primary objective lies in optimizing the microstructure to enhance key performance parameters such as the J_c and T_c. Studies indicate that rational selection of doping elements combined with precise control of processing conditions can significantly improve performance. For instance, the addition of Ag under low oxygen partial pressure promotes c-axis texturing and suppresses pore formation, which is beneficial for increasing J_c [61]. Partial substitution of Ca^{2+} by an appropriate amount of Na^+ (e.g., x = 0.10) can elevate J_c to 1.35×10^5 A/cm² at 10 K, while at x = 0.075, T_c is optimized to approximately 93.3 K. This enhancement is primarily attributed to increased grain size, improved texture, and a reduction in secondary Bi-2201 phase content [62]. Nane et al. confirmed that Na doping (x = 0.075) can raise J_c in textured ceramics to 1.38×10^5 A/cm² at 10 K [63].

As shown in Figure 7 [64], when Na doping is low ($x \leq 0.02$), the sample is mainly the Bi-2212 phase with good texture. However, when doping increases to 0.05 at% or higher, clear peaks of the non-superconducting Bi-2201 phase appear (▽). This shows that too much Na causes the Bi-2212 phase to break down during sintering, leading to harmful phase separation. This separation reduces the superconducting phase, breaks grain connections, and can weaken the benefits of low doping. Therefore, Na doping works best within a certain range, enough to improve pinning, but not so much that it causes bad phase separation.

 doi:10.20944/preprints202603.1268.v1

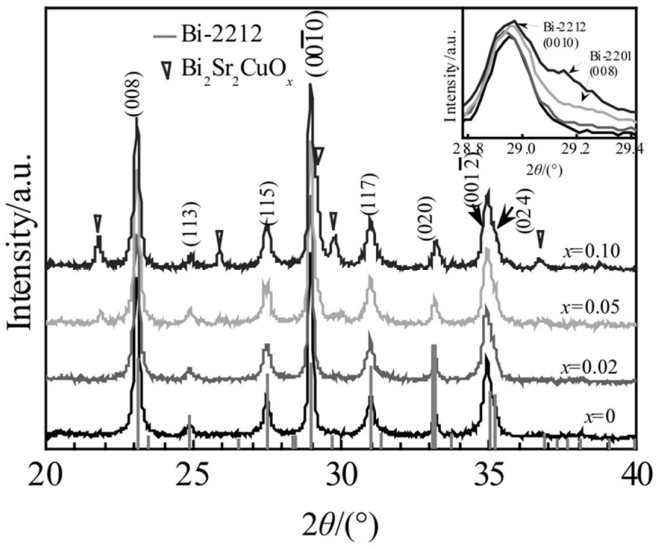

Figure 7. XRD patterns of SPS-sintered Bi-2212 bulks with different Na doping contents (x = 0, 0.02, 0.05, 0.10 at%). Adapted from [64] (CC BY 4.0).

Moreover, Pb doping, when its content exceeds a certain threshold (e.g., x ≥ 0.4), induces a distinct phase separation characterized by a two-phase lamellar microstructure. The interfaces in this structure are oriented perpendicular to the CuO_2 planes and can effectively suppress thermally activated flux flow, leading to a notable enhancement of both J_c and the irreversibility field H_{irr} [65].

However, doping may also lead to detrimental phase separation or introduce impurity phases that degrade performance. For example, Ag can react with the oxide melt during partial melting to form Ag-rich Cu dendritic phases (such as $Ag_{0.98}Cu_{0.02}$ and $Ag_{0.24}Cu_{0.76}$) [66]. These dendritic phases may disrupt the connectivity between Bi-2212 grains, constituting a microstructural factor that limits J_c. Excessive partial substitution of Cu^{2+} by Ti^{4+} introduces impurity phases such as $SrTiO_3$ and alters lattice parameters, subsequently causing significant reductions in J_c and T_c [67]. The origin of these performance variations lies in the profound influence of Ag doping on the phase equilibria, solidification pathway, and microstructural evolution within the Bi-2212 system. The addition of Ag markedly lowers the primary crystallization temperature of the 2212 phase and modifies the type and stability of equilibrium solid phases within the melt (e.g., promoting the formation of (11) and (21) phases while suppressing the stability of the (9115) phase) [68]. Concurrently, Ag dissolves into the liquid phase, lowering the system's melting point and reducing the Cu content in the melt [69]. These changes subsequently affect texture formation, densification, and intergranular connectivity, ultimately optimizing the superconducting properties.

Pb doping has long been recognized for its favorable improvements in the Bi-2212 phase [70]. By substituting Bi^{3+} with Pb^{2+}, it increases the formal Cu valency and thus the number of hole charge carriers [71], leading to a sizable enhancement in J_c under magnetic field at an optimal Pb content of x = 0.16 [72]. Simultaneously, Pb doping significantly reduces the melting point of the Bi-2212 phase and alters its decomposition path upon melting, causing it to decompose into a liquid phase and (Sr, Ca)CuO_2 in air [73]. Microstructural analyses of high-performance Bi-2212 conductors further reveal that after melt processing, Bi-2212 grains commonly exhibit a composition characterized by Bi excess and alkaline-earth deficiency, along with numerous Bi-2201 intergrowth structures and amorphous/nanocrystalline layers. These microstructural features are closely linked to the conductor geometry (e.g., round wires) and their specific melt-processing history [74].

 doi:10.20944/preprints202603.1268.v1

Figure 8 presents the Scanning Electron Microscopy (SEM) images of the surface morphologies. Platelet-like grains, with sizes around 10 μm, which dependent on the synthesis and sintering procedures, are observed in the reference sample. The influence of doping on morphology is found to follow two opposite trends depending on the dopant element. Moderate doping with Zn or Ti is associated with an increase in platelet size. At higher Ti concentrations, as in sample Ti10, a notably compact structure is formed, characterized by merged layers and intersected by only a few tubular cavities. The surfaces of the platelets appear clean and smooth, with neat borders. In contrast, samples doped with Y and Nd exhibit smaller flat flakes, approximately 2 μm in size. The flake size is observed to decrease with increasing dopant content, approaching a granular aspect ratio in sample Y05.

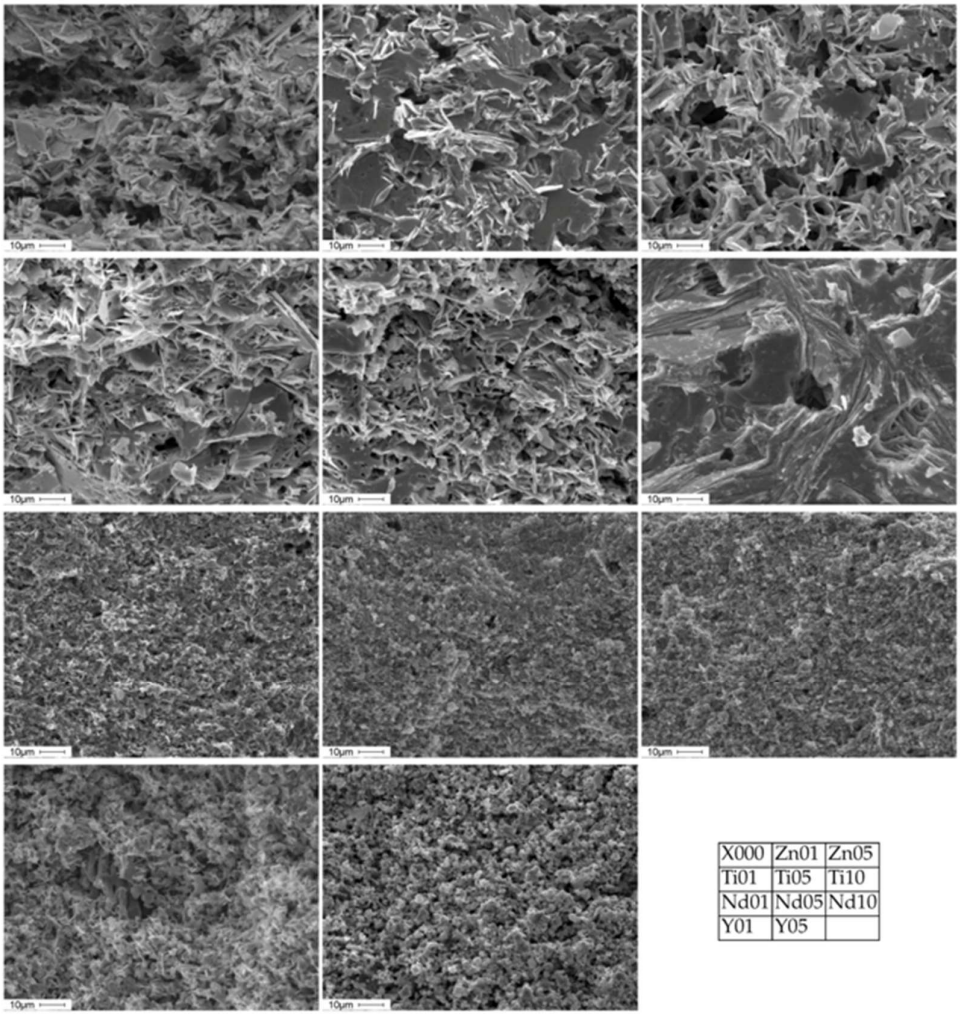

Figure 8. SEM micrographs demonstrating the distinct morphological evolution of Bi-2212 grains induced by different dopant elements. Reproduced from [75] under the terms of the Creative Commons Attribution license.

The preceding discussion elucidates, from a mechanistic perspective, the influence of various elemental dopants on the phase separation and properties of Bi-2212. To provide a more direct comparison of the quantitative enhancement in superconducting current-carrying capability achieved by different doping strategies, Table 3 summarizes the self-field J_c data for representative doped Bi-2212 samples. As can be seen, appropriate doping with Na or K significantly enhances J_c, particularly at low temperatures (10 K or 4.2 K), where the improvement can reach up to an order of magnitude. This offers clear experimental evidence for optimizing Bi-2212 performance through compositional design.

 doi:10.20944/preprints202603.1268.v1

Table 3. Self-field J_c of doped Bi-2212 at 4.2 K and 10 K, respectively.

Sample	Temperature	Dopant	J_c (A/cm²)	
$Bi_2Sr_2Ca_{1-x}Na_xCu_2O_{8+\delta}$	10 K	Undoped	0.81×10^5	[62]
		0.1-Na	1.33×10^5	
$Bi_2Sr_2Ca_{1-x}Na_xCu_2O_{8+\delta}$	10 K	Undoped	0.34×10^5	[63]
		0.075-Na	1.38×10^5	
$Bi_2Sr_{2-x}CaCu_2O_{8+\delta}$	4.2 K	Undoped	3.6×10^4	[76]
		0.02-Yb	4.6×10^4	
$Bi_2Sr_2Ca_{1-x}K_xCu_2O_{8+\delta}$	4.2 K	Undoped	4.4×10^4	[77]
		0.05-K	12.8×10^4	

In summary, the precise doping with elements such as Ag, Na, and Pb enables the thermodynamic and kinetic regulation of the phase equilibria and solidification pathway in the Bi-2212 system, thereby optimizing its microstructure and superconducting properties. In addition to compositional design, processing parameters are also recognized as exerting a decisive influence on phase separation behavior, which will be discussed in detail in the following section.

2.2.2. Thermal Processing of Bi-2212 Powders for Enhanced Connectivity

The fabrication of Bi-2212 round wires is typically carried out by the powder-in-tube (PIT) method, in which Bi-2212 precursor powder is packed into silver tubes and subsequently drawn into multifilamentary wires. The quality of the starting powder, including its phase purity, particle size, and flowability, is considered to have a direct influence on the fill factor, filament uniformity, and ultimately the critical current density of the final wire [78]. Processing parameters critically govern phase separation and superconducting properties in Bi-2212. For powder-in-tube (PIT) multifilamentary round wires, atmospheric pressure (1 bar) heat treatment leads to poor connectivity from bubbles and pores formed during melting, severely limiting J_c. Conversely, applying an overpressure heat treatment (100 bar) effectively suppresses bubble formation and enhances Bi-2212 phase densification. This leads to an eightfold increase in the engineering current density (J_e) and successfully generates an additional field of 2.6 T within a 31.2 T background field, demonstrating its potential for high-field magnet applications [5]. Further research by Nachtrab et al. on optimizing Bi-2212/Ag wire performance via a single-stack multifilamentary process revealed that increasing the superconductor fill factor (to 35-40%) and reducing the single filament diameter (below 18 μm) significantly enhance both J_c and n value, while the influence of filament spacing (s/d) is relatively minor [78]. This provides crucial guidance for wire design aimed at MRI applications.

Oxygen partial pressure and temperature schedule during heat treatment also profoundly affect phase composition and microstructure. Comparative studies by Holesinger et al. on melt processing under oxygen and argon atmospheres showed that melting in argon followed by annealing in oxygen yields a more uniform microstructure compared to melting and annealing entirely in oxygen. This process forms dominant $Bi_2Sr_{3-x}Ca_xO_7$ and Cu_2O/CuO eutectic structures, with the final annealing step recovering the 2212 phase with a relatively high T_c of approximately 88-89 K [79]. In-depth research by Marinkovic et al. demonstrated that within the temperature range of 865-900 °C, the peritectic melting of Bi-2212 exhibits two distinct regimes. Below 890 °C, incomplete melting occurs, forming a small amount of fine second phases such as $(Sr, Ca)_{14}Cu_{24}O_{41}$ and $Bi_5Sr_{11}Ca_5O_4$. However, insufficient oxygen uptake results in a low superconducting volume fraction. Above 890 °C, complete melting takes place. Although this generates a larger quantity of coarse second phases, sufficient oxygen absorption significantly increases the proportion of the Bi-2212 phase, consequently achieving a J_c as high as 1000 A/cm² at 77 K in self-field [80]. Investigations of crystal growth in the Bi-Sr-Ca-Cu-O system by Kameneva et al. revealed that slow cooling after high temperature (≥ 1000 °C) homogenization leads to the quantitative formation of a red eutectic structure composed of a $Bi_{16}(Sr, Ca)_{14}O_{38}$ matrix with Cu_2O rod-like precipitates. The formation of this structure indicates the presence of numerous 2201-type stacking faults within the grown 2212 crystals, revealing a connection between the solidification path and crystal defects [81]. Finally, research by Imayev et al. showed that

 doi:10.20944/preprints202603.1268.v1

applying a quasi-hydrostatic pressure of about 10 MPa can raise the melting point of Bi-2212 by approximately 60 ℃ and alter its decomposition products. At atmospheric pressure, a Cu-poor (Sr, Ca)CuO_2 phase forms, whereas under pressure, a Cu-rich (Sr, Ca)$_{14}Cu_{24}O_{41}$ phase is produced. This indicates that pressure enhances the thermal stability of the material by suppressing structural instability, likely through the locking of apical oxygen within the lattice [82].

In summary, a range of strategies has been developed to optimize the phase evolution and superconducting performance of Bi-2212. As discussed throughout this section, the introduction of dopants such as Ag, Na, and Pb has been widely employed to regulate phase equilibria and refine the resulting microstructure [61–66,68–73]. Concurrently, careful optimization of heat treatment parameters, including atmosphere control, overpressure processing, and precise temperature scheduling, has been demonstrated to be critical for enhancing densification and intergranular connectivity [5,78–81]. For instance, doping with Ag or TiO2, combined with optimized thermal processing, has been shown to effectively refine the microstructure, reduce porosity, and enhance the critical current density in high-field applications [5,67,82,83]. These complementary approaches, rooted in both compositional design and process engineering, form the foundation for achieving reliable, high-performance Bi-2212 conductors suitable for demanding magnet applications.

3. Powder Processing of FeSeTe: From Elemental Mixtures to Superconducting Phases

In the preparation of Fe(Se,Te) superconductors, the precise handling of precursor powders is established as a fundamental prerequisite for achieving optimal final performance. Initially, the weighing and mixing of high-purity elemental powders (Fe, Se, Te) must be conducted within a high-purity inert atmosphere (e.g., an argon-filled glove box) to rigorously avoid oxidation or hydration. Even minor oxygen or moisture contamination can introduce magnetic impurities such as Fe_2O_3, which are detrimental to superconductivity [84–86]. Mechanical processing of the powder mixture significantly influences the kinetics of subsequent reactions. The application of high-energy ball milling (HEBM) has been demonstrated to directly form Fe-Se-Te ternary compound precursors via mechanical alloying, while concurrently refining particle size and shortening atomic diffusion paths. This approach fundamentally mitigates volume expansion and porosity caused by the volatilization of liquid Se and Te during conventional sintering. Consequently, the density of the sintered body is substantially increased from 2.29 g/cm^3 to 5.61 g/cm^3, enabling the fabrication of high-performance samples at reduced sintering temperatures and durations [87].

The emergence of iron-based superconductors (IBSCs) has stimulated extensive investigation into their synthesis, motivated by their exceptional upper critical fields and high critical current densities [88–91]. Owing to its structural simplicity, high upper critical field, and low toxicity, the Fe(Se, Te) system, a prominent member of the “11” family, is considered a promising system for applied studies [92–97]. Bulk solidified Fe(Se, Te) materials have been the subject of extensive research as promising candidates for practical applications.

Similar to REBCO, the superconducting properties of FeSeTe bulk materials, such as J_c and flux pinning capability, are also strongly influenced by their microstructure. Due to the presence of a miscibility gap in the FeSeTe system [98,99], macroscopic phase separation readily occurs during solidification from the high-temperature melt, resulting in the formation of Se-rich and Te-rich phase regions [10,100,101].

The superconducting performance of the material is ultimately dictated by its microstructural architecture, where the morphology of phase separated regions and the degree of chemical homogeneity critically determine the efficacy of flux pinning and the current carrying capacity across grain boundaries [8,9,100,101]. Furthermore, the solidification pathway and subsequent thermal processing significantly influence the precipitation behavior of secondary phases (e.g., the hexagonal δ-FeSe or Fe_7Se_8 phase), the elemental distribution, and the concentration of interstitial iron, which serve as pivotal parameters for optimizing J_c and pinning performance [8,99,102–105].

 doi:10.20944/preprints202603.1268.v1

This chapter provides a systematic review of the phase separation phenomena in FeSeTe materials during solidification. It focuses on the strategies for its control through composition design and processing parameters, and analyzes the influence of the resulting microstructures on superconducting properties.

3.1. Powder Modification via Doping and Stoichiometry Control

FeSeTe polycrystalline materials are typically prepared by solid-state reaction using elemental Fe, Se, and Te powders as starting materials. The mixing and ball milling conditions, including milling time, speed, and medium, are known to influence the homogeneity of the elemental distribution. This homogeneity, in turn, affects the formation of the superconducting phase and the extent of phase separation during subsequent sintering [8,101]. The phase composition and distribution in FeSeTe materials can be precisely manipulated through adjustments in stoichiometry or the introduction of dopant elements, thereby enabling subsequent optimization of their superconducting properties.

The Se/Te ratio serves as a critical factor in determining the phase composition of the $FeSe_{1-x}Te_x$ system. An optimal ratio near x = 0.5 facilitates a homogeneous microstructure dominated by the superconducting Fe(Se, Te) phase and minimizes the formation of detrimental secondary phases [102,106,107].

The incorporation of a new element or compound is an effective approach for tailoring the microstructure of FeSeTe. By introducing a new element or specific compounds, it is possible to optimize grain structure, suppress the formation of detrimental phases, and introduce effective flux pinning centers. Consequently, the superconducting properties, particularly J_c, can be significantly enhanced.

The effects of transition metal doping on the superconducting properties of the Fe(Se, Te) system have been extensively investigated. In a systematic study on $Fe_{0.95}TM_{0.05}Se_{0.5}Te_{0.5}$, for instance, Zhang et al. reported that doping with Mn or Co only slightly modifies T_c, even leading to a minor enhancement [108]. In contrast, the introduction of Ni or Cu completely suppresses superconductivity. Gawryluk et al. systematically evaluated the doping behavior of multiple elements, including Co, Ni, Cu, Mn, Zn, Mo, Cd, and In, in $FeTe_{1-x}Se_x$ single crystals. Their results indicated that only Co, Ni, and Cu can effectively substitute for Fe sites in the lattice [109], whereas the other elements predominantly formed secondary-phase inclusions, consequently modifying the matrix composition and affecting T_c. Building on this, the study by Liu et al. further demonstrates that trace Co doping (<1 at %) in $FeSe_{0.4}Te_{0.6}$ single crystals successfully incorporates Co at the Fe sites, resulting in a slight contraction of the lattice parameters and a significant enhancement of J_c under high magnetic fields [110].

In addition to transition metal dopants, non-metal element doping has proven to be highly effective in tailoring the microstructure and superconducting performance. A prominent example is fluorine doped Fe(Se, Te), where F doping is found to induce a distinctive dual-oscillation effect [9]. Firstly, the microstructure of the undoped sample is typical of phase separation during melting. Remarkably, F doping triggers a dramatic change, leading to a pearlite-like morphology, defined by the periodic alternation of the β-Fe(Se, Te) and δ-Fe(Se, Te) phases. This self-organization is a direct consequence of altered phase formation kinetics induced by the fluorine. Secondly, a chemical compositional oscillation occurs due to inhomogeneous distribution of Se and Te within the β-phase. These dual oscillations collectively change the primary flux pinning mechanism from surface pinning to $\Delta\kappa$ pinning, thereby promoting a substantial improvement in both J_c and H_{c2}.

Furthermore, the addition of FeF_2 transforms the phase-separation morphology from typically irregular, flower-like patterns into a macroscopically ordered structure characterized by submillimeter-scale striations aligned along the c-axis [10]. As shown in Figure 9, the backscattered electron images clearly illustrate this morphological transition: the FeF_2-free sample exhibits a typical flower-like Se-rich phase distribution (Figure 9a), while the FeF_2-added sample displays a regular, striated morphology with alternating Se-rich and Te-rich phases (Figure 9b). Comprising the well-

 doi:10.20944/preprints202603.1268.v1

defined phases $FeSe_{0.6}Te_{0.4}$ and $FeSe_{0.4}Te_{0.6}$, this configuration enhances phase purity, leading to the induction of a $\Delta\kappa$ pinning mechanism. Consequently, a superior superconducting performance is achieved, characterized by simultaneous enhancements in T_c, H_{c2}, and J_c.

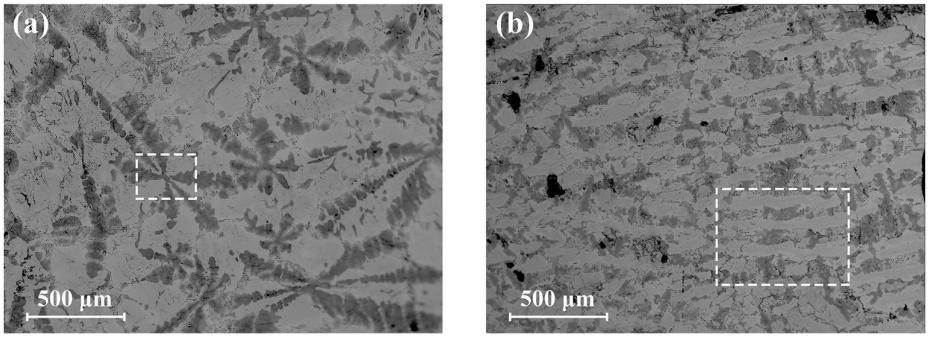

Figure 9. BSE images of the (a) FeF_2-Free sample and (b) FeF_2-added sample, all polished along the c-axis. From Ref. [10] under CC BY-NC-ND 4.0.

The significant improvement in current carrying capacity is directly evidenced by the magnetic field dependence of J_c. As shown in Figure 10, at 4.2 K, the FeF_2-added sample with macroscopically ordered phase separation exhibits substantially higher J_c values than its FeF_2-free counterpart across the entire field range, especially under high magnetic fields (e.g., 7 T). This demonstrates that the ordered phase separation structure effectively enhances flux pinning and mitigates the suppression of J_c by magnetic fields.

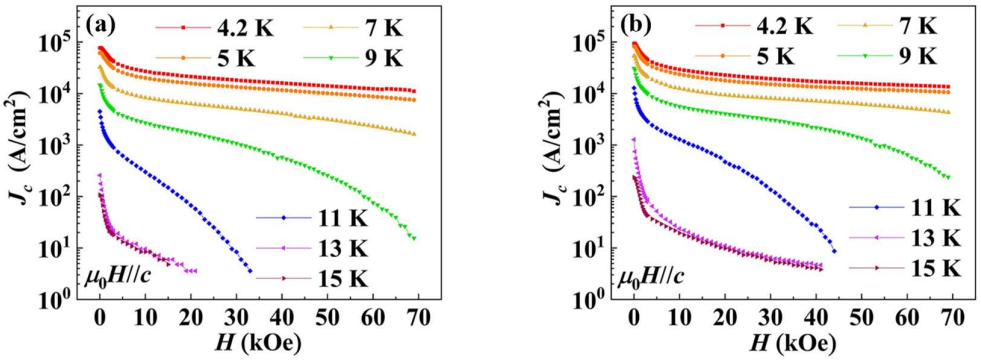

Figure 10. Magnetic field dependence of J_c at 4.2 K for (a) FeF_2-free and (b) FeF_2-added Fe(Se, Te) samples. Data in panels (a) and (b) are replotted from panels (c) and (d) of Figure 6 in Ref. [10], CC BY-NC-ND 4.0.

The underlying change in flux pinning mechanism is revealed by analyzing the normalized pinning force. As shown in Figure 11, the scaling behavior of the pinning force (f_p) as a function of reduced field (H/H_{irr}) differs significantly between the two types of samples. For the common phase separated sample (Figure 11a), the dominant pinning mechanism shifts from point pinning to surface pinning as temperature increases. In contrast, the sample with macroscopically ordered phase separation (Figure 11b) exhibits the emergence of $\Delta\kappa$ pinning at low temperatures, and the transition to surface pinning is notably delayed. This indicates that the regular, stoichiometry-defined phase boundaries in the ordered structure create a more effective and thermally stable pinning landscape.

 doi:10.20944/preprints202603.1268.v1

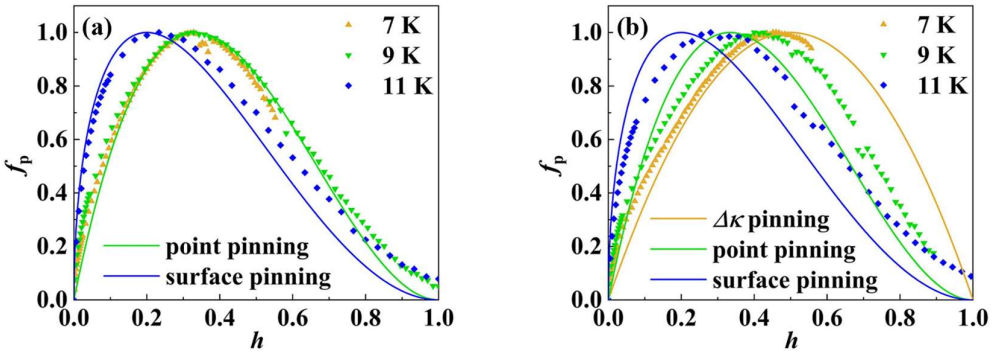

Figure 11. Normalized pinning force f_p as a function of reduced field H/H_{irr} for (a) FeF_2-free and (b) FeF_2-added Fe(Se,Te) samples at various temperatures. Data in panels (a) and (b) are replotted from panels (e) and (f) of Figure 6 in Ref. [10], CC BY-NC-ND 4.0.

A co-doping strategy employing Ag and O was developed by Liu et al. to concurrently improve intergranular connectivity and flux pinning in Fe(Se, Te) polycrystals [111]. Ag segregated at grain boundaries to enhance current transport, while oxygen from SeO_2 mitigated the detrimental interstitial Fe by forming Fe_2O_3 precipitates that acted as effective pinning centers. This approach resulted in an approximate 4.7-fold increase in J_c at 8 T and 5 K for the 0.05 Ag/O Co-doped sample. Similarly, Chen et al. reported that trace Sn doping in $FeSe_{0.5}Te_{0.5}$ bulks promoted the formation of a near-stoichiometric superconducting phase and suppressed secondary phases, leading to improved microstructural homogeneity [104]. This structural refinement resulted in a self-field J_c of 9×10^3 A/cm^2 at 4.3 K and a retained J_c of 4×10^2 A/cm^2 at 5 T, indicating a significant enhancement of in-field current transport. To provide a more intuitive comparison of the impact of different doping strategies on the current carrying performance of FeSeTe superconductors, Figure 12 summarizes the J_c-H curve for representative doped samples at 5 K. The curves clearly illustrate that the Co-doped [110] sample exhibits superior field dependence performance, maintaining the highest J_c values across the entire field range (0-5 T). In contrast, the other doped samples (e.g., F-doped [9,10], Cl-doped [15], and Ag/O co-doped [111]) show varying degrees of field suppression. While their J_c degradation trends share a broadly similar downward trajectory, differences in absolute J_c values are evident, particularly at intermediate and high fields. This direct comparison confirms the unique efficacy of Co doping in creating flux-pinning centers and demonstrates that the other dopants, despite showing some improvement, are less effective than Co in mitigating field induced suppression of J_c.

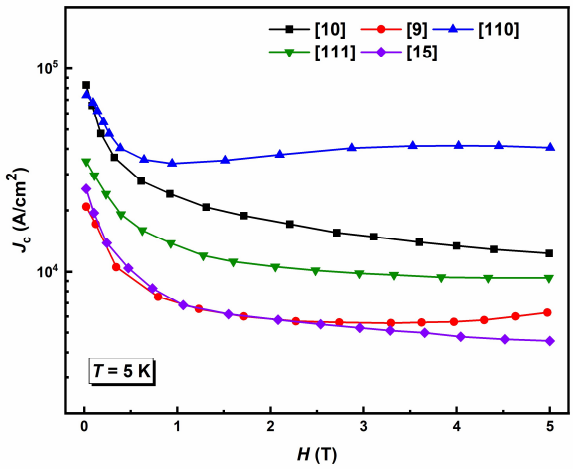

Figure 12. Comparison of the J_c for various doping strategies in FeSeTe superconductors.

 doi:10.20944/preprints202603.1268.v1

Collectively, the doping strategies discussed above operate through a common underlying principle: the induction of structural and compositional modulations within the Fe(Se,Te) matrix. As demonstrated with elements such as F, Sn, Co, or Cl, these modulations effectively alter the flux pinning landscape, introducing novel pinning mechanisms (e.g., $\Delta\kappa$ pinning) or refining the existing pinning architecture [9,10,15,110,112]. Consequently, a substantial enhancement in high-field performance, particularly in terms of J_c, has been consistently achieved across various doping systems. Figure 12 provides a direct comparison of the influence of different doping strategies on the magnetic field dependence of J_c at 5 K. The data clearly illustrate that while all modifications enhance performance to some degree, Co doping exhibits a superior ability to mitigate field-induced suppression of J_c across the entire measured field range. To allow a more systematic evaluation of the performance differences among the doping systems, Table 4 summarizes the J_c values of representative FeSeTe polycrystalline samples at self-field and at 5 T, covering both undoped and chemically doped cases. These data offer a quantitative basis for comparing the effectiveness of the various doping approaches.

Table 4. Summary of J_c values at self-field and 5 T for undoped and doped FeSeTe polycrystalline samples from literature [9,10,15,104,110,111].

Polycrystal	Temperature	Doping Condition	J_c (0T, A/cm²)	J_c (5T, A/cm²)	
$Co_xFe_{1-x}Se_{0.4}Te_{0.6}$	5 K	Undoped	1.8×10^4	0.4×10^4	[110]
		0.003-Co	7.4×10^4	4.1×10^4	
$FeSe_{0.5-x}Te_{0.5}F_x$	5 K	Undoped	6.3×10^4	1.1×10^4	[10]
		FeF_2-0.025	8.2×10^4	1.3×10^4	
$FeSe_{0.5-x}Te_{0.5}F_x$	5 K	Undoped	1.9×10^4	0.3×10^4	[9]
		FeF_2-0.025	2.1×10^4	0.6×10^4	
$FeSe_{0.5}Te_{0.5}$	4.3 K	Undoped	0.9×10^4	6.3	[104]
		Sn-5wt%	0.6×10^4	430.9	
$FeSe_{0.5-x}Te_{0.5}Cl_x$	5 K	Undoped	1.9×10^4	0.3×10^4	[15]
		$FeCl_2$-0.025	2.5×10^4	0.5×10^4	
$FeSe_{0.5-x}Te_{0.5}(SeO_2+Ag)_x$	5 K	Undoped	1.5×10^4	0.3×10^4	[111]
		0.05 Ag+SeO_2	3.4×10^4	0.9×10^4	

3.2. Sintering and Annealing: Transforming FeSeTe Powders into High-Performance Bulks

The solidification pathway, which encompasses cooling rate, thermal gradient, and post-processing heat treatment, exerts a decisive influence on the phase distribution and microstructure evolution in FeSeTe superconductors.

In the Fe(Te, Se) system, rapid cooling or high growth rates promote elemental segregation of Te and Se at the microscale, resulting in phase separation into Te-rich and Se-rich nanodomains. The work of Masi et al. confirms that rapid cooling promotes Te/Se elemental segregation in melt-processed $FeSe_{0.5}Te_{0.5}$, giving rise to a phase-separated microstructure consisting of a Te-rich tetragonal matrix and Se-rich dendrites [8]. This compositional and structural heterogeneity directly degrades the superconducting performance, evidenced by a reduction in T_c. Terao et al. further demonstrated through single-crystal growth experiments that a large temperature gradient induces an inhomogeneous distribution of Se and Te, leading to the broadening of XRD peaks and a degradation in the sharpness of the superconducting transition [106]. Besides, a comparative study by Galluzzi et al. on Fe(Se, Te) samples synthesized via the Bridgman and Self-flux methods revealed that the Bridgman-grown sample, benefiting from a slower cooling rate and superior temperature control, exhibits a higher J_c and a more homogeneous microstructure [113]. The 2020 study by Masi et al. further elucidated that while rapid quenching from high temperature preserves the high-temperature hexagonal phase and leads to a coarse core-shell microstructure detrimental to superconducting performance, optimized annealing (e.g., at 440 °C for 740 h) can significantly enhance the current carrying capability: the J_c at 4.2 K increased from 0.6×10^4 A/cm² to 1×10^4 A/cm²

 doi:10.20944/preprints202603.1268.v1

at self-field, and from 0.1 × 10^4 A/cm^2 to 0.3 × 10^4 A/cm^2 at 5 T, accompanied by a markedly reduced field dependence [100]. Moreover, nanoscale Te/Se phase separation, manifested as hexagonal phase regions and compositional fluctuations, has been linked to rapid crystal growth in Fe(Se, Te) systems [114,115]. In conclusion, controlling the temperature gradient and cooling rate during directional solidification presents an effective strategy for tailoring elemental distribution and grain orientation, thereby mitigating macro-segregation and optimizing superconducting performance.

Thermal processing, including annealing and cyclic sintering, is a critical post-processing step for optimizing the phase purity, microstructure. Investigations confirm that the annealing temperature is a decisive parameter for controlling the phase composition and elemental distribution within the material. For instance, annealing at 550 ℃ effectively mitigates compositional inhomogeneity within the primary tetragonal phase and enhances superconducting uniformity [99]. In contrast, prolonged annealing at 680 ℃ facilitates the transformation of dendritic precipitates from a core-shell to a lamellar morphology. This structural evolution promotes elemental interdiffusion, induces the separation of distinct superconducting phases, and significantly improves both the high-field J_c and flux pinning capability [101]. The evolution of secondary phases is also governed by the annealing temperature. For example, a high-temperature hexagonal phase can transform into either a trigonal Fe_7Se_8-type or an orthorhombic $FeTe_2$-type structure [100]. Multiple sintering cycles have been shown to effectively reduce the content of non-superconducting secondary phases and enhance the superconducting volume fraction. As reported by Miao et al., three-cycle sintering yields the best performance, achieving a self-field J_c of 1.77 × 10^4 A/cm^2 at 4 K [116]. Simultaneously, heat treatment is utilized to control the size and distribution of magnetic secondary phases, such as $Fe_7(Te, Se)_8$, alleviate structural stress, and facilitate elemental homogenization [114,117]. These processes collectively inhibit harmful phase separation, which in turn results in a synergistic improvement of the superconducting and magnetic performance. In summary, a rationally designed heat treatment process facilitates the formation of the primary FeSeTe phase and reduces the content of non-superconducting phases, resulting in a systematic improvement of the overall superconducting properties [99–101].

4. The Role of Boron and Magnesium Powders in Defining MgB_2 Microstructure

The quality of the boron precursor is a primary determining factor. High-purity (e.g., 99%) amorphous boron powders with a nanoscale particle size are fundamental for achieving superior superconducting properties [118]. Nanosized boron facilitates the formation of fine MgB_2 grains, which is crucial because grain boundaries are the dominant flux pinning centers in this material [11,119,120]. A higher density of grain boundaries directly enhances J_c, particularly in high magnetic fields. Conversely, the use of lower-purity boron powders (e.g., 90% or 96%) leads to the introduction of oxide impurities like B_2O_3 and results in larger, less reactive particles, significantly degrading the final sample performance even after purification attempts [118]. The crystallinity of boron (amorphous versus crystalline) also dictates its reactivity during the in-situ reaction [11]. The magnesium precursor is equally important; precise control of the Mg:B molar ratio, ideally 1:2, is required to avoid the formation of non-superconducting secondary phases such as MgB_4 or residual Mg.

The reactivity of magnesium necessitates stringent control over oxygen exposure. MgO is an almost ubiquitous secondary phase in MgB_2 samples. While a fine dispersion of nanoscale MgO particles can contribute to flux pinning [11,121], excessive formation of this phase is detrimental. Bulk MgO segregates at grain boundaries, severely disrupting intergranular connectivity, broadening the superconducting transition, and reducing the effective cross-sectional area for supercurrent flow. Therefore, handling of Mg powder in an inert atmosphere (e.g., an argon-filled glovebox) is imperative to minimize oxidation [122].

Mechanical milling of precursor powders is a widely adopted strategy to enhance performance. High-energy ball milling refines particle size, increases surface area, and introduces crystallographic defects and internal strain. These defects can evolve into effective pinning centers in the final sintered

 doi:10.20944/preprints202603.1268.v1

material. The milling parameters must be optimized carefully. Insufficient milling yields limited benefits, whereas excessive milling can introduce contaminants from the milling media (e.g., Fe, W, C) and cause particle agglomeration, ultimately degrading performance. The use of a process control agent, such as toluene during wet milling, is often employed to prevent excessive cold welding and oxidation, resulting in finer and cleaner powders. An alternative and highly effective method for particle refinement is ultrasonication. This technique can fracture inexpensive microcrystalline boron into nanoscale particles without the contamination risks associated with ball milling, leading to enhanced grain boundary pinning in the final MgB_2 bulk.

MgB_2 exhibits significant potential for medium-field applications due to its relatively high T_c (~39 K), simple crystal structure, low raw material cost, and absence of weak-link problems at grain boundaries [123–126]. In contrast to complex oxide superconductors such as REBCO, MgB_2 is typically synthesized via solid-state reaction. Its superconducting properties are strongly influenced by the microstructure, particularly the grain size, density, and distribution of secondary phases [119,127]. Although the synthesis of MgB_2 typically does not involve complex peritectic reactions, phase separation during its solidification from high-temperature melts (or precursor reactions) remains critical, as it governs the grain boundary characteristics, distribution of secondary phases, and ultimately, the current carrying and flux-pinning capabilities. Therefore, precise control of phase separation through tailored composition and processing is essential for optimizing the superconducting performance of MgB_2, particularly its J_c in high magnetic fields.

This introduction will establish the focus of this chapter, optimizing the superconducting properties of MgB_2 by controlling phase separation through tailored composition and processing.

4.1. Doping and Nano-Additives: Engineering Flux Pinning at the Powder Stage

MgB_2 superconductors are typically synthesized via solid-state reaction, either from Mg and B powders (in-situ route) or from pre-reacted MgB_2 powder (ex-situ route). The characteristics of the boron powder, including whether it is amorphous or crystalline, its purity, and its particle size, are considered to play a decisive role in determining the reaction kinetics, phase formation, and ultimately the superconducting properties [127]. Likewise, dopants such as SiC, C, or Y_2O_3 are introduced through powder mixing or ball milling, and the dispersion homogeneity of these nano-additives is known to directly influence the density and distribution of flux pinning centers [16,17]. The introduction of specific dopants or second-phase nanoparticles represents one of the most effective strategies for tailoring the microstructure of MgB_2 and inducing beneficial phase separation.

Research indicates that even at low doping levels ($x > 0.04$), macroscopic phase separation occurs in carbon-doped MgB_2. Papagelis et al. confirmed via AC magnetic susceptibility measurements that the $MgB_{2-x}C_x$ ($0 \le x \le 0.1$) system exhibits multi-phase coexistence at $x > 0.04$, while still maintaining full diamagnetism [128]. This phenomenon was initially demonstrated by Maurin et al. using high-resolution synchrotron X-ray diffraction, which revealed extremely low carbon solid solubility and the presence of multiple AlB_2-type structural phases with distinct lattice parameters a when $x > 0.04$, although a single-step superconducting transition was still observed in DC magnetization. Subsequent studies have shown that controlled nanoscale carbon doping can effectively introduce flux pinning centers, substantially enhancing J_c [120]. Through Raman spectroscopy, Arvanitidis et al. found that at $x > 0.04$, the disorder-related ω peak intensity increases significantly, and the full width at half maximum of the E_2g mode reflects the competing effects of weakened electron-phonon coupling and enhanced disorder [129]. Regarding J_c improvement, Yeoh et al. demonstrated that combining nano-carbon doping with high-temperature sintering (900 - 1000 ℃) can enhance the magnetic J_c of MgB_2 bulks by two orders of magnitude at 5 K and 8 T, and by 33 times at 20 K and 5 T, while transport I_c in wires increases by 5.7 times at 4.2 K and 12 T, primarily due to carbon substitution at boron sites and the homogeneous dispersion of nanoparticles [120]. In addition, Hassan et al. reported that 5% Cu doping significantly improves the response slope, detection limit, and stability of MgB_2-based electrochemical sensors, extending its application to non-superconducting fields [130]. Furthermore, Ning and Shi et al. respectively demonstrated that Ag or

 doi:10.20944/preprints202603.1268.v1

Sn doping promotes the formation of Mg-Ag or Mg-Sn eutectic liquid phases at relatively low temperatures (around 470 ℃), accelerating MgB_2 phase formation and facilitating low-temperature densification and performance optimization [131,132]. Finally, Adriano et al. compared Mn and C doping effects via angle-resolved photoemission spectroscopy, revealing that both cause Fermi surface contraction of the σ band, but Mn leads to more pronounced T_c suppression due to magnetic impurity-induced Abrikosov-Gorkov spin-flip scattering that disrupts Cooper pairs [133].

Compared to SiC-added samples with equivalent nominal content, the (Si+C) samples exhibit greater contraction along the a-axis and a higher carbon substitution level (x), leading to more significant T_c suppression and lattice distortion [134]. Although carbon substitution enhances the potential for high-field performance, magnetic measurements reveal that at an addition level of 5 wt.%, SiC doping yields a higher J_c at both 5 K and 20 K. This is attributed to the formation of effective flux pinning centers such as Mg_2Si generated by the reaction of SiC, while avoiding excessive Mg loss and the formation of secondary phases caused by intense reactions in the (Si+C) sample. Consequently, SiC is considered a superior dopant for low-field applications around 20 K. Dou et al. achieved synergistic substitution of Si and C at B sites through SiC nanoparticle doping [17], introducing high density dislocations and nanoscale impurities within grains as effective pinning centers, which significantly enhanced current carrying performance. Under optimal doping, the sample reached a J_c of 1.8×10^4 A/cm² at 20 K and 4 T, with a T_c suppression of only 2.6 K. Sumption et al. [135] doped wires with 10 mol% SiC and applied a 900 ℃ heat treatment, effectively increasing the upper critical field and intra-grain pinning strength. This resulted in an H_{irr} of 18 T at 4.2 K and a maximum pinning force density (F_P) as high as 20 GN/m³, primarily due to enhanced electron scattering and the formation of effective pinning centers introduced by SiC. Yamamoto et al. [136] pointed out that whether B_4C or SiC is used as the carbon source, their influence on the superconducting properties of MgB_2 generally depends on the carbon substitution level for boron, specifically manifested as a-axis contraction, T_c decrease, and high-field J_c improvement. However, SiC enables effective carbon doping even under low-temperature synthesis conditions, whereas B_4C relies more on high-temperature reactions, giving SiC a processing advantage. Hapipi et al. [16] demonstrated that co-adding 5 wt.% SiC and MgH_2 in ex-situ MgB_2 can suppress high-temperature decomposition of MgB_2, thereby improving the purity of the main superconducting phase and enhancing intergranular connectivity. Their study revealed that the co-doped sample exhibits a significantly refined and densified microstructure compared to samples doped with SiC alone. This microstructural optimization, characterized by finer grain size and improved connectivity, provides continuous pathways for supercurrent flow and is a key factor contributing to the high self-field J_c of 2.25×10^4 A/cm² achieved at 20 K [16].

Further analysis indicates that the enhanced performance also originates from the in-situ formation of numerous nanoscale features within the co-doped sample, such as whisker-like MgO nanostructures and Mg_2Si secondary phases [16]. These nanoscale precipitates act as effective flux pinning centers, substantially enhancing the current-carrying capability under applied magnetic fields. Therefore, the co-doping of SiC and MgH_2 enables the synergistic optimization of both intergranular connectivity, which governs macroscopic current percolation, and nanoscale pinning centers, which govern microscopic flux pinning, leading to an overall improvement in the superconducting properties of MgB_2.

The efficacy of various doping schemes in enhancing the self-field current carrying capacity of polycrystalline MgB_2 is quantitatively compared in Table 5. As summarized in Table 5, the baseline J_c of undoped MgB_2 polycrystals typically falls within the order of 10^5 A/cm². Doping with C [120] or SiC [17,134] generally leads to a moderate improvement, elevating J_c to the range of 2.7×10^5 to 7.6×10^5 A/cm². A particularly striking enhancement is observed with Ti [137] substitution in the $Mg_{1-x}Ti_xB_2$ system, where a J_c of 13×10^5 A/cm² is achieved for x = 0.1. Similarly, the addition of Y_2O_3 [138] nanoparticles also yields a significant boost in J_c. This compilation underscores that tailored chemical additions, which modify phase separation during processing, are a direct and effective route to engineering a higher density of flux-pinning defects and thereby improving the superconducting

 doi:10.20944/preprints202603.1268.v1

performance. A comparison of the field-dependent J_c behavior (Figure 13) reveals distinct trends beyond the self-field values listed in Table 5. The Ti-doped sample exhibits the highest zero-field J_c, but its performance degrades most sharply with increasing magnetic field. In contrast, the other doped systems (e.g., C, SiC, and Y_2O_3) show remarkably similar and more gradual J_c decay profiles over the 0-5 T range. This indicates that, while Ti doping creates exceptionally effective pinning centers at low fields, the microstructures engineered by other additives provide more stable flux-pinning landscapes under applied magnetic fields.

Table 5. Self-field J_c at 20 K for MgB_2 polycrystals with various chemical additions.

Polycrystal	Doping Condition	J_c (0T, A/cm²)	
$MgB_{2-x}C_x$	Undoped	2.5×10^5	[120]
	0.1-C	2.7×10^5	
MgB_2	Undoped	2.1×10^5	[134]
	3 wt%-SiC	3.9×10^5	
	3 wt%-(Si+C)	2.1×10^5	
$MgB_2(SiC)_x$	Undoped	6.6×10^5	[17]
	0.115- SiC	7.6×10^5	
$Mg_{1-x}Ti_xB_2$	Undoped	1.9×10^3	[137]
	0.1-Ti	13×10^5	
MgB_2	Undoped	1.0×10^5	[138]
	10 wt%-Y_2O_3	3.4×10^5	

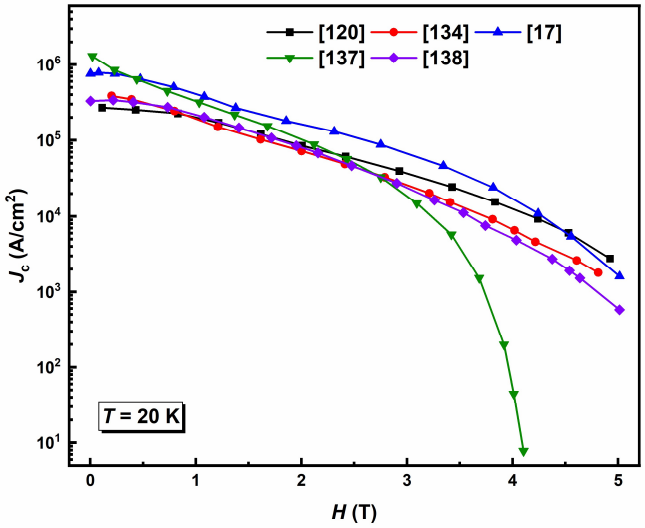

Figure 13. Magnetic field dependence of J_c at 20 K for MgB_2 polycrystals with various chemical additions.

In summary, compositional design strategies, such as the introduction of SiC nanoparticles or the co-doping of SiC with MgH_2, can effectively generate a high density of nanoscale flux-pinning centers in MgB_2. These strategies, when coupled with the concurrent improvement in intergranular connectivity, enable the synergistic optimization of its superconducting properties. Beyond the specific doping strategies discussed above, a broader range of approaches has been explored to optimize the MgB_2 microstructure. In particular, the incorporation of metallic additives and the application of low-temperature activated sintering processes have been shown to play a crucial role in facilitating the formation of the superconducting phase, refining grain structure, and mitigating oxidation and porosity [12,16,17,138]. These effects are fundamental to achieving high-performance bulk materials.

 doi:10.20944/preprints202603.1268.v1

The sintering temperature, even under high external pressure, remains a decisive factor in determining the phase composition and structural quality of MgB_2. Figure 14 illustrates this dependency through XRD patterns of bulk MgB_2 samples processed at temperatures ranging from 700 to 1100 ℃ under approximately 5 GPa pressure [139]. As the temperature increases, the MgB_2 peaks sharpen and shift slightly, indicating improved crystallinity and lattice relaxation. However, beyond 900 ℃, distinct diffraction peaks of MgB_4 and MgO emerge, signaling the onset of significant decomposition of the superconducting phase. This temperature-induced phase separation underscores the delicate balance required in processing: excessive temperature stabilizes non-superconducting phases, degrading the overall current-carrying capability.

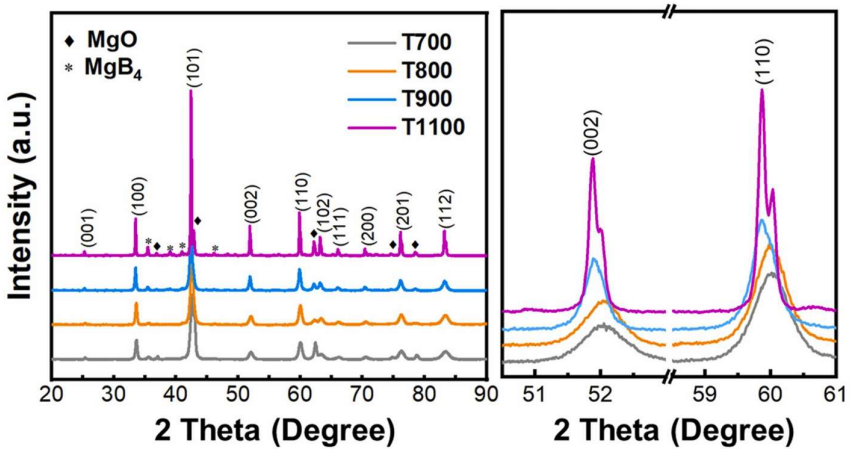

Figure 14. XRD patterns of MgB_2 bulk samples sintered at different temperatures under high pressure (~5 GPa). The inset highlights the evolution of the (002) and (110) peaks. Adapted from [139] under the terms of the CC BY 4.0 license.

4.2. Sintering Routes: From Powder Compacts to Dense Superconducting Bulks

The synthesis and post-processing parameters critically determine the phase purity, grain size, and distribution of secondary phases in MgB_2.

Among these, low-temperature sintering technology is regarded as a highly promising approach due to its ability to effectively suppress MgO formation and reduce grain size, thereby offering the potential to enhance J_c. Huang et al. developed an innovative low-temperature sintering route utilizing $Mg(BH_4)_2$ as a precursor [140]. Their work successfully demonstrated the synthesis of MgB_2 superconductors at temperatures as low as 400-500 ℃. The microstructural evolution was found to be critically dependent on both sintering temperature and duration. At the initial stage (e.g., 400 ℃ for 2 h), the microstructure consisted of fine, isolated grains with poor intergranular connectivity. As the temperature increased and sintering time was prolonged, the grains gradually coarsened and coalesced. Ultimately, after sintering at 500 ℃ for 54 hours, a dense microstructure with blurred grain boundaries and excellent intergranular connectivity was achieved [140].

In the fabrication of MgB_2, the influence of different processing routes on phase separation and superconducting properties has been extensively investigated. Noudem et al. produced bulk MgB_2 via spark plasma sintering (SPS), which exhibits levitation forces comparable to YBCO at low temperatures, demonstrating its potential for magnetic levitation applications [121]. Hapipi et al. reported that co-addition of 5 wt.% SiC and 6 mol% MgH_2 at a high sintering temperature of 1000 ℃ significantly enhanced J_c of ex-situ MgB_2, reaching 22,517 A/cm² at 20 K and self-field, while increasing the MgB_2 phase fraction to 43.0% [16]. Innovative processing routes that combine shaping and densification steps are emerging to overcome the limitations of conventional sintering. One promising approach is the integration of Laser Powder Bed Fusion (L-PBF) with SPS [141]. As shown in Figure 15, this method begins with the L-PBF fabrication of a porous MgB_2 preform with defined geometry. Subsequent SPS treatment using a sacrificial SiC matrix densifies the preform while

 doi:10.20944/preprints202603.1268.v1

preserving its macroscopic shape. The resulting microstructure exhibits a characteristic lamellar morphology with well-connected grains, which is crucial for establishing continuous superconducting current paths. This hybrid process demonstrates the feasibility of manufacturing complex-shaped MgB_2 components without severely compromising the superconducting transition, which remains near 38 K.

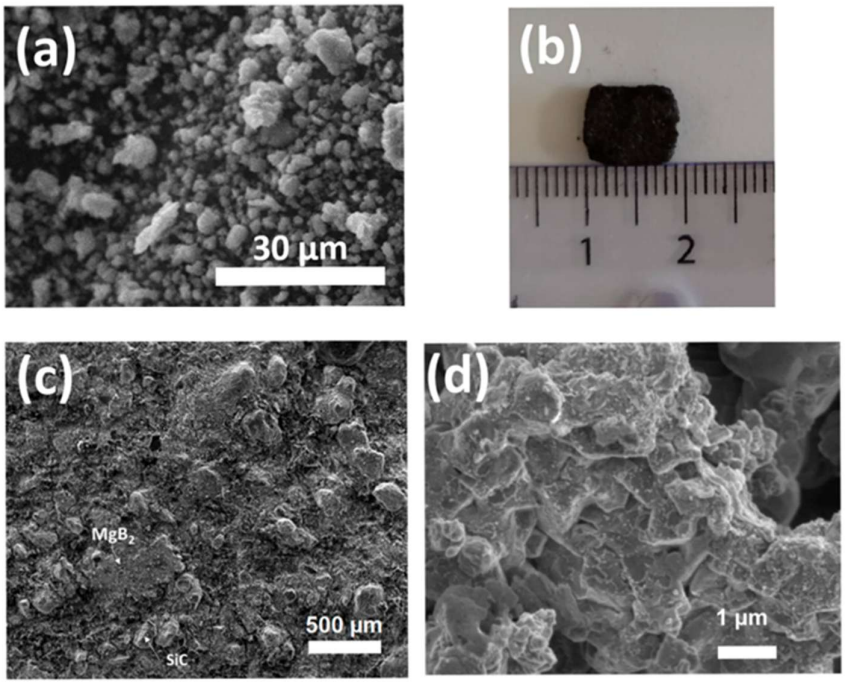

Figure 15. Micrographs of an MgB_2 sample processed by combined L-PBF and SPS: (a) starting powder, (b) sintered cuboid preform, (c) surface morphology after SPS, and (d) detailed view of the sintered microstructure. Adapted from Sklyarova et al. [141] under the terms of the CC BY 4.0 license.

Through prolonged self-sintering at 900 ℃ for 96 h, Shimada et al. examined the microstructure connectivity of ex-situ bulk MgB_2, revealing that, despite improved packing factor, platelet-like pores and MgO agglomeration restrict current flow, with the optimal sample achieving only 21% connectivity [142]. Birajdar et al. compared various powder-in-tube (PIT) processed MgB_2 wires and tapes, showing that mechanically alloyed samples exhibit superior high-field J_c due to high density and fine grains, while SiC addition in in-situ tapes helps retain and form Mg_2Si, improving flux pinning [143]. Appropriate post-annealing is crucial for optimizing PIT-fabricated MgB_2 tapes. Matsumoto et al. demonstrated that short - time annealing at 600 ℃ for stainless steel-sheathed MgB_2 tapes effectively heals microcracks induced by cold rolling and enhances intergranular electrical connectivity, leading to an order-of-magnitude increase in J_c under high fields (e.g., 10 T) [144]. Furthermore, Sklyarova et al. combined laser powder bed fusion (L-PBF) with SPS to fabricate complex-shaped MgB_2 components with a superconducting transition temperature of 38 K, highlighting the potential of additive manufacturing for superconducting applications [141].

Based on the above findings, the superconducting properties of MgB_2 are closely linked to phase separation phenomena occurring during processing. The superior high-field J_c observed in optimally processed MgB_2 can be directly correlated with the nanoscale defect structure introduced during sintering. Figure 16 presents a direct comparison using transmission electron microscopy [139]. In a sample sintered at 900 ℃ under high pressure, a dense network of dislocations is clearly visible within the MgB_2 grains. These lattice defects act as effective flux-pinning centers, enhancing the material's ability to retain superconductivity in applied magnetic fields. In contrast, the microstructure of a sample processed at 1100 ℃ shows significantly coarsened grains with few remaining dislocations,

 doi:10.20944/preprints202603.1268.v1

as most defects have been annealed out. This loss of intragranular pinning sites explains the rapid degradation of J_c at high fields for samples sintered at excessively high temperatures, highlighting the critical importance of preserving beneficial crystal defects during processing.

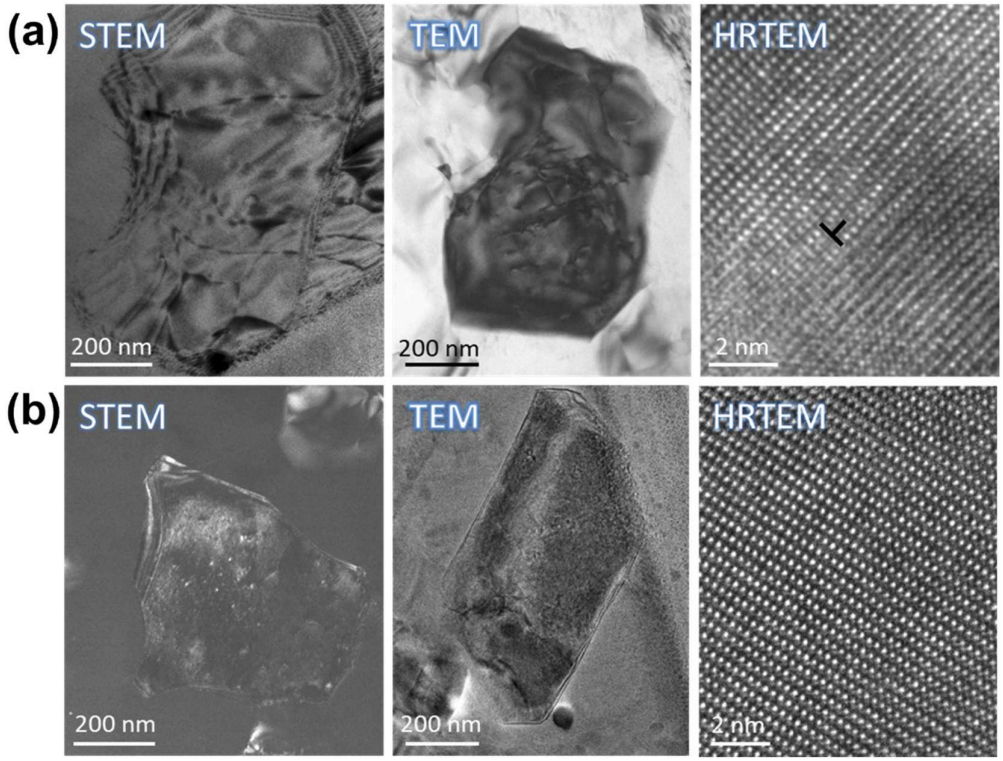

Figure 16. TEM images of MgB_2 grains sintered at (a) 900 ℃ and (b) 1100 ℃ under high pressure. Dense dislocations in (a) provide strong flux pinning, while defects are annealed out in (b). Adapted from [139] under the terms of the CC BY 4.0 license.

Through composition design, such as the introduction of nano-additives like SiC, a high density of nanoscale secondary phases can be in situ generated to serve as effective flux pinning centers. Meanwhile, precise control of sintering parameters helps suppress the formation of detrimental phases (e.g., coarse MgO) and promotes fine, uniformly distributed phase separation, along with optimized grain boundary structure. Future research may focus on the synergistic effects of multiple dopants, the development of novel nano-additives, and more refined process control tailored to practical conductor forms such as wires and tapes, aiming to further enhance the performance of MgB_2 across broader temperature and magnetic field ranges.

In summary, Table 6 [16,122,140,142,145] compiles J_c values of MgB_2 bulk superconductors fabricated under different processing conditions. The compiled data demonstrate that tailoring sintering parameters and incorporating selected nano-additives can markedly improve the current carrying capacity. These findings collectively underscore the decisive role of processing pathway design in refining the material's microstructure, thereby enhancing both intergranular current percolation and flux pinning effectiveness. The performance of MgB_2 is critically determined by the microstructure shaped during processing. Figure 17 compares the magnetic field dependence of J_c at 20 K for samples fabricated via the distinct routes listed in Table 6. Notably, the sample processed by Field-Assisted Sintering Technique (FAST) [145] exhibits the highest self-field J_c but a rapid decline with increasing field. Conversely, specimens prepared through optimized conventional sintering or precursor based low-temperature routes demonstrate more gradual J_c decay, indicative of a more robust and field-stable pinning architecture. This highlights that the choice of processing pathway

 doi:10.20944/preprints202603.1268.v1

governs not only the density of pinning centers but also their effectiveness under applied magnetic fields.

Table 6. Comparison of J_c values for MgB_2 bulk superconductors processed under different conditions. Data are extracted from literature [16,122,140,142,145] for measurements at 20 K and applied fields of 0 T or 0.2 T.

Sample Composition/Description	Processing Conditions	J_c (A/cm²)	
Unmodified ex-situ MgB_2	Self-sintering at 900 °C, 48 h	2.8×10^5	[142]
ex-situ MgB_2 + 6 wt.% Mg	FAST at 900 °C, 5 min	2.6×10^9	[145]
MBH500-54 ($Mg(BH_4)_2$ precursor)	Sintered at 500 °C, 54 h	2.9×10^5	[140]
MgB_2 + 2.8 wt.% C (C-coated B)	Sintered at 805 °C, 3 h	3.8×10^5	[122]
MgB_2 + 5 wt.% SiC + 3 mol% MgH_2	Ex-situ, 1000 °C, 1 h	2.3×10^4	[16]

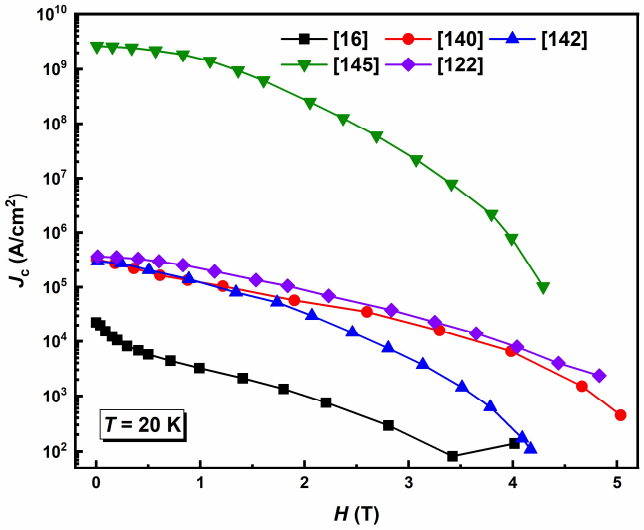

Figure 17. Magnetic field dependence of J_c at 20 K for MgB_2 polycrystals fabricated via the processing routes summarized in Table 6.

5. Conclusions and Outlook

In this review, the critical role of solidification-induced phase separation in governing the microstructure and superconducting properties of four major practical superconductors, namely REBCO, Bi-2212, FeSeTe, and MgB_2, has been systematically examined. Across these distinct material systems, a consistent principle can be identified: the path from powder precursors to final performance is fundamentally shaped by phase separation phenomena. The characteristics of the starting powders, including particle size, purity, morphology, and doping homogeneity, are considered to set the initial conditions for all subsequent microstructural evolution.

The discussion emphasizes two primary and interrelated microstructural control strategies, compositional design and process engineering. For REBCO superconductors, the refinement of RE-211 precipitates is achieved through the addition of elements or compounds such as CeO_2, Pt, and BaO_2. Superior microstructural homogeneity over the TSMG process is provided by the TSIG technique, which avoids peritectic decomposition. In the case of Bi-2212, enhanced phase stability and material densification are obtained by doping with Ag, Na, or Pb, followed by optimized melting and ultra-high pressure heat treatments. Regarding FeSeTe materials, disordered phase separation can be transformed into an ordered layered structure via strategic doping with elements like F or Co. This structural ordering introduces effective $\Delta\kappa$ flux-pinning centers, while subsequent controlled cooling and annealing processes are crucial for achieving homogeneity. Within the MgB_2 system, improved grain connectivity and a high density of nanoscale flux-pinning defects are simultaneously

 doi:10.20944/preprints202603.1268.v1

introduced. This is accomplished by the incorporation of nanoparticles such as SiC alongside advanced sintering techniques, including SPS or FAST processing routes.

The development of next-generation practical superconductors requires an integrated advancement across several fundamental areas. A deeper predictive understanding of the thermodynamics and kinetics governing solidification-phase separation is essential. This must be coupled with the design of novel microstructures through multi-component doping and nanocomposite approaches to achieve synergistic flux-pinning effects. Concurrently, processing routes must be developed with explicit focus on scalability, reproducibility, and performance under realistic high-field operating conditions. The integration of precise compositional control with such advanced and standardized processing pathways is anticipated to significantly enhance the performance of key superconductor systems. This holistic approach, rooted in a fundamental understanding of microstructural evolution, is critical for unlocking their full technological potential.

Author Contributions: Zhenguo Zhang was responsible for literature search, data collection, analysis, and drafting of the manuscript. Minghui Tang conceptualized the research framework and critically revised the manuscript for intellectual content and structure. Hao Zhou and Wei Ren participated in preliminary literature sorting. Shuhua Yang and Dongliang Wang provided academic guidance. Yanwei Ma provided resource support, supervised the research, and approved the final version. All authors reviewed and agreed to the submitted manuscript.

Funding: This research was partially supported by the National Natural Science Foundation of China (Grant Nos. 52588101, 52377032, 52377033), the CAS Superconducting Research Project under Grant No. SCZX-0103, the Science and Technology Research Foundation of Institute of Electrical Engineering of Chinese Academy of Sciences under Grant No. IEERF250204, Beijing Municipal Science & Technology Commission, Administrative Commission of Zhongguancun Science Park No. Z251100003625029, the International Partnership Program of Chinese Academy of Sciences (Grant No. 116GJHZ2023005MI).

Conflicts of Interest: The authors declare that they have no known competing financial interests or personal relationships that could have appeared to influence the work reported in this paper.

References

1. Namburi, D.K.; Shi, Y.H.; Cardwell, D.A. The processing and properties of bulk (RE)BCO high temperature superconductors: current status and future perspectives. Supercond. Sci. Technol. 2021, 34, 053002. http://dx.doi.org/10.1088/1361-6668/abde88
2. Jetybayeva, A.; Mukanova, A.; Nurpeissova, A.; Bakenov, Z.; Petrykin, V.; Lee, S. REBCO superconductors by pulsed laser deposition : Key innovations and large-scale applications. Iscience. 2025, 28, 113260. http://dx.doi.org/10.1016/j.isci.2025.113260
3. Shiohara, Y.; Endo, A. Crystal growth of bulk high-Tc superconducting oxide materials. Mater. Sci. Eng.: R: Rep. 1997, 19, 1-86. http://dx.doi.org/doi.org/10.1016/s0927-796x(96)00198-2
4. MacManus-Driscoll, J.L.; Wimbush, S.C. Processing and application of high-temperature superconducting coated conductors. Nat. Rev. Mater. 2021, 6, 587-604. http://dx.doi.org/10.1038/s41578-021-00290-3
5. Larbalestier, D.C.; Jiang, J.; Trociewitz, U.P.; Kametani, F.; Scheuerlein, C.; Dalban-Canassy, M.; Matras, M.; Chen, P.; Craig, N.C.; Lee, P.J.; et al. Isotropic round-wire multifilament cuprate superconductor for generation of magnetic fields above 30 T. Nat. Mater. 2014, 13, 375-381. http://dx.doi.org/10.1038/nmat3887
6. Bruzzone, P.; Fietz, W.H.; Minervini, J.V.; Novikov, M.; Yanagi, N.; Zhai, Y.H.; Zheng, J.X. High temperature superconductors for fusion magnets. Nucl. Fusion. 2018, 58, 103001. http://dx.doi.org/10.1088/1741-4326/aad835
7. Scanlan, R.M.; Malozemoff, A.P.; Larbalestier, D.C. Superconducting materials for large scale applications. Proc. IEEE. 2004, 92, 1639-1654. http://dx.doi.org/10.1109/JPROC.2004.833673
8. Masi, A.; Alvani, C.; Augieri, A.; Bellusci, M.; Celentano, G.; Marzi, G.D.; Fabbri, F.; Zignani, C.F.; Barbera, A.L.; Padella, F.; et al. Phase separation and microstructure in superconducting FeSe1-xTex materials. IEEE Trans. Appl. Supercond. 2018, 28, 1-5. http://dx.doi.org/10.1109/TASC.2018.2791547

 doi:10.20944/preprints202603.1268.v1

9. Liu, J.X.; Zhang, S.N.; Li, M.; Sang, L.N.; Li, Z.; Cheng, Z.X.; Zhao, W.Y.; Feng, J.Q.; Li, C.S.; Zhang, P.X.; et al. Boosting superconducting properties of Fe(Se, Te) via dual-oscillation phenomena induced by fluorine doping. ACS Appl. Mater. Interfaces. 2019, 11, 18825-18832. http://dx.doi.org/10.1021/acsami.9b02469
10. Sun, Q.; Xu, Z.T.; Dong, C.H.; Huang, H.; Wang, D.L.; Zhang, X.P.; Ma, Y.W. Macroscopically ordered phase separation: A new strategy for improving the superconducting performance in Fe(Se, Te). Mater. Today Adv. 2023, 17, 100354. http://dx.doi.org/10.1016/j.mtadv.2023.100354
11. Muralidhar, M.; Shadab, M.; Srikanth, A.S.; Jirsa, M.; Jacques, N. Review on high-performance bulk MgB2 superconductors. J Phys D: Appl Phys 2024, 57, 053001. http://dx.doi.org/10.1088/1361-6463/ad039a
12. Ma, Z.Q.; Liu, Y.C. Low-temperature synthesis of MgB2 superconductors. Int. Mater. Rev. 2011, 56, 267-286. http://dx.doi.org/10.1179/1743280411y.0000000002
13. Babu, N.H.; Shi, Y.H.; Pathak, S.K.; Dennis, A.R.; Cardwell, D.A. Developments in the processing of bulk (RE)BCO superconductors. Physica C. 2011, 471, 169-178. http://dx.doi.org/10.1016/j.physc.2010.12.006
14. Namburi, D.K.; Shi, Y.H.; Palmer, K.G.; Dennis, A.R.; Durrell, J.H.; Cardwell, D.A. Control of Y-211 content in bulk YBCO superconductors fabricated by a buffer-aided, top seeded infiltration and growth melt process. Supercond Sci Technol 2016, 29, 034007. http://dx.doi.org/10.1088/0953-2048/29/3/034007
15. Liu, J.; Zhang, S.; Sang, L.; Li, M.; Zhao, W.; Li, Z.; Cheng, Z.; Liu, L.; Feng, J.; Li, C.; et al. Enhancement of superconducting properties in polycrystalline Fe(Se, Te) via a dual coordination effect. Scr. Mater. 2019, 169, 19-22. http://doi.org/10.1016/j.scriptamat.2019.04.029
16. Mohd Hapipi, N.; Chen, S.K.; Shaari, A.H.; Awang Kechik, M.M.; Lim, K.P.; Kamarudin, A.N.; Shabdin, M.K.; Tan, K.B.; Lee, O.J.; Miryala, M. Enhancing critical current density in ex-situ MgB2 via high-temperature sintering with SiC and MgH2 additives. Physica B. 2025, 718, 417882. http://doi.org/10.1016/j.physb.2025.417882
17. Dou, S.X.; Pan, A.V.; Zhou, S.; Ionescu, M.; Liu, H.K.; Munroe, P.R. Substitution-induced pinning in MgB2 superconductor doped with SiC nano-particles. Supercond Sci Technol 2002, 15, 1587. http://dx.doi.org/10.1088/0953-2048/15/11/317
18. Antončík, F.; Sedmidubský, D.; Jiříčková, A.; Lojka, M.; Hlásek, T.; Růžička, K.; Jankovský, O. Thermodynamic properties of stoichiometric non-superconducting phase Y2BaCuO5. Materials. 2019, 12, 3163. http://doi.org/10.3390/ma12193163
19. Nariki, S.; Sakai, N.; Murakami, M.; Hirabayashi, I. High critical current density in RE–Ba–Cu–O bulk superconductors with very fine RE2BaCuO5 particles. Physica C. 2004, 412-414, 557-565. http://doi.org/10.1016/j.physc.2004.01.078
20. Namburi, D.K.; Shi, Y.H.; Palmer, K.G.; Dennis, A.R.; Durrell, J.H.; Cardwell, D.A. An improved top seeded infiltration growth method for the fabrication of Y-Ba-Cu-O bulk superconductors. J Eur Ceram Soc 2016, 36, 615-624. http://dx.doi.org/10.1016/j.jeurceramsoc.2015.09.036
21. Ouerghi, A.; Moutalbi, N.; Noudem, J.G.; M'Chirgui, A. The influence of slow cooling on Y211 size and content in single-grain YBCO bulk superconductor through the infiltration-growth process. Physica C. 2017, 534, 37-44. http://doi.org/10.1016/j.physc.2017.01.003
22. Alade, I.O.; Rahaman, M.S.; Qahtan, T.F. A comprehensive review of superconductivity research productivity. J. Supercond. Novel Magn. 2022, 35, 2621-2637. http://dx.doi.org/10.1007/s10948-022-06326-1
23. Maeda, H.; Yanagisawa, Y. Recent developments in high-temperature superconducting magnet technology (Review). IEEE Trans. Appl. Supercond. 2014, 24, 4602412. http://dx.doi.org/10.1109/tasc.2013.2287707
24. Bussmann-Holder, A.; Keller, H. High-temperature superconductors: underlying physics and applications. Zeitschrift fur Naturfor-schung Sect. B J. Chem. Sci. 2020, 75, 3-14. http://dx.doi.org/10.1515/znb-2019-0103
25. Bednorz, J.G.; Müller, K.A. Possible high Tc superconductivity in the Ba−La−Cu−O system. Z. Phys. B: Condens. Matter. 1986, 64, 189-193. http://dx.doi.org/10.1007/BF01303701
26. Cardwell, D.A.; Shi, Y.H.; Numburi, D.K. Reliable single grain growth of (RE)BCO bulk superconductors with enhanced superconducting properties. Supercond Sci Technol 2020, 33, 024004. http://dx.doi.org/10.1088/1361-6668/ab627d
27. Thoma, M.; Shi, Y.; Dennis, T.; Durrell, J.; Cardwell, D. Effect of Y-211 particle size on the growth of single grain Y–Ba–Cu–O bulk superconductors. J. Cryst. Growth. 2015, 412, 31-39. http://doi.org/10.1016/j.jcrysgro.2014.11.037

 doi:10.20944/preprints202603.1268.v1

28. Kim, S.-J.; Kim, H.-G. Effects of 211 inclusions on zone melt-textured (RE/Y)–Ba–Cu–O superconductors. Physica C. 2000, 338, 110-114. http://dx.doi.org/10.1016/S0921-4534(00)00211-2
29. Kuchárová, V.; Diko, P.; Volochová, D.; Rajňák, M. Influence of additives on microstructural evolution and superconducting performance of EuBCO-Ag compounds. J Alloys Compd 2025, 1040, 183581. https://doi.org/10.1016/S0921-4534(00)00211-2
30. Xu, C.; Hu, A.; Sakai, N.; Izumi, M.; Hirabayashi, I. Effect of BaO2 and fine Gd2BaCuO7−δ addition on the superconducting properties of air-processed GdBa2Cu3O7−δ. Supercond Sci Technol 2005, 18, 229. http://dx.doi.org/10.1088/0953-2048/18/3/004
31. Shi, Y.; Hari Babu, N.; Iida, K.; Cardwell, D.A. Properties of GdBCO bulk superconductors melt-processed in air using a Mg-doped Nd–Ba–Cu–O generic seed crystal. Supercond Sci Technol 2007, 20, 38. http://dx.doi.org/10.1088/0953-2048/20/1/007
32. Zhai, W.; Shi, Y.; Durrell, J.H.; Dennis, A.R.; Zhang, Z.; Cardwell, D.A. Processing and properties of bulk Y-Ba-Cu-O superconductors fabricated by top seeded melt growth from precursor pellets containing a graded CeO2 composition. Cryst Growth Des 2015, 15, 907-914. http://dx.doi.org/10.1021/cg501724y
33. Zhao, W.; Shi, Y.; Radušovská, M.; Dennis, A.R.; Durrell, J.H.; Diko, P.; Cardwell, D.A. Comparison of the effects of platinum and CeO2 on the properties of single grain, Sm–Ba–Cu–O bulk superconductors. Supercond Sci Technol 2016, 29, 125002. http://dx.doi.org/10.1088/0953-2048/29/12/125002
34. Shlyk, L.; Nenkov, K.; Krabbes, G.; Fuchs, G. Melt-processed YBCO with Pt or Ce additions: comparison of pinning behavior. Physica C. 2005, 423, 22-28. http://doi.org/10.1016/j.physc.2005.03.019
35. Cui, Y.; Yang, W. Enhanced performance of GdBCO bulk superconductors by doping a new kind of YGdBa4CuNbOy nanoparticles. Supercond Sci Technol 2024, 37, 035002. http://dx.doi.org/10.1088/1361-6668/ad1e32
36. Shi, Y.; Babu, N.H.; Iida, K.; Cardwell, D.A. The effect of very high barium content in the precursor on the properties of GdBCO single grain bulk superconductors. J Mater Res 2009, 24, 10-18. http://dx.doi.org/10.1557/JMR.2009.0032
37. Li, Z.; Ida, T.; Miki, M.; Izumi, M. Trapped flux behavior in melt-growth GdBCO bulk superconductor under off-axis field cooled magnetization. IEEE Trans. Appl. Supercond. 2017, 27, 1-4. http://dx.doi.org/10.1109/TASC.2016.2639281
38. Lo, W.; Cardwell, D.A.; Dewhurst, C.D.; Leung, H.T.; Chow, J.C.L.; Shi, Y.H. Controlled processing and properties of large Pt-doped Y–Ba–Cu–O pseudocrystals for electromagnetic applications. J Mater Res 1997, 12, 2889-2900. http://dx.doi.org/10.1557/JMR.1997.0383
39. Shi, Y.; Hari Babu, N.; Iida, K.; Yeoh, W.K.; Dennis, A.R.; Cardwell, D.A. The influence of Gd-2411(Nb) on the superconducting properties of GdBCO/Ag single grains. Supercond Sci Technol 2009, 22, 075025. http://dx.doi.org/10.1088/0953-2048/22/7/075025
40. Hari Babu, N.; Iida, K.; Cardwell, D.A. Flux pinning in melt-processed nanocomposite single-grain superconductors. Supercond Sci Technol 2007, 20, S141. http://dx.doi.org/10.1088/0953-2048/20/9/S05
41. Muralidhar, M.; Koblischka, M.R.; Diko, P.; Murakami, M. Enhancement of Jc by 211 particles in ternary (Nd0.33Eu0.33Gd0.33)Ba2Cu3Oy melt-processed superconductors. Appl Phys Lett 2000, 76, 91-93. http://dx.doi.org/10.1063/1.125666
42. Zhai, W.; Shi, Y.; Durrell, J.H.; Dennis, A.R.; Cardwell, D.A. The influence of Y-211 content on the growth rate and Y-211 distribution in Y-Ba-Cu-O single grains fabricated by top seeded melt growth. Cryst Growth Des 2014, 14, 6367-6375. http://dx.doi.org/10.1021/cg501135q
43. Endo, A.; Chauhan, H.S.; Egi, T.; Shiohara, Y. Macrosegregation of Y2Ba1Cu1O5 particles in Y1Ba2Cu3O7−δ crystals grown by an undercooling method. J Mater Res 1996, 11, 795-803. http://dx.doi.org/10.1557/JMR.1996.0096
44. Hlásek, T.; Shi, Y.; Durrell, J.H.; Dennis, A.R.; Namburi, D.K.; Plecháček, V.; Rubešová, K.; Cardwell, D.A.; Jankovský, O. Cost-effective isothermal top-seeded melt-growth of single-domain YBCO superconducting ceramics. Solid State Sci. 2019, 88, 74-80. http://doi.org/10.1016/j.solidstatesciences.2018.12.008
45. Abulaiti, A.; Yang, W.M.; Wu, T.T.; Cui, Y.L. The effect of pre-sintering and high-temperature infiltration on the properties of single-domain YBCO bulk superconductors by the Y+011 top-seeded infiltration growth process. Supercond Sci Technol 2023, 36, 025005. http://dx.doi.org/10.1088/1361-6668/acaa65

 doi:10.20944/preprints202603.1268.v1

46. Kuchárová, V.; Diko, P.; Volochová, D.; Antal, V.; Lojka, M.; Hlásek, T.; Plecháček, V. Microstructure and superconducting properties of bulk EuBCO-Ag with and without holes. J. Eur. Ceram. Soc. 2022, 42, 6533-6541. http://doi.org/10.1016/j.jeurceramsoc.2022.06.081
47. Reddy, E.S.; Rajasekharan, T. Fabrication of textured REBa2Cu3O7/RE2BaCuO5 (RE = Y, Gd) composites by infiltration and growth of RE2BaCuO5 preforms by liquid phases. Supercond. Sci. Technol. 1998, 11, 523. http://dx.doi.org/10.1088/0953-2048/11/5/014
48. Namburi, D.K.; Shi, Y.; Palmer, K.G.; Dennis, A.R.; Durrell, J.H.; Cardwell, D.A. A novel, two-step top seeded infiltration and growth process for the fabrication of single grain, bulk (RE)BCO superconductors. Supercond Sci Technol 2016, 29, 095010. http://dx.doi.org/10.1088/0953-2048/29/9/095010
49. Matsumoto, K.; Mele, P. Artificial pinning center technology to enhance vortex pinning in YBCO coated conductors. Supercond Sci Technol 2010, 23, 014001. http://dx.doi.org/10.1088/0953-2048/23/1/014001
50. Goyal, A.; Kang, S.; Leonard, K.J.; Martin, P.M.; Gapud, A.A.; Varela, M.; Paranthaman, M.; Ijaduola, A.O.; Specht, E.D.; Thompson, J.R.; et al. Irradiation-free, columnar defects comprised of self-assembled nanodots and nanorods resulting in strongly enhanced flux-pinning in YBa2Cu3O7−δ films. Supercond Sci Technol 2005, 18, 1533. http://dx.doi.org/10.1088/0953-2048/18/11/021
51. Yang, W.M.; Zhou, L.; Feng, Y.; Zhang, P.X.; Zhang, C.P. The effect of temperature gradient on the morphology of YBCO bulk superconductors by melt texture growth processing. J Alloys Compd 2006, 415, 276-279. http://doi.org/10.1016/j.jallcom.2005.08.007
52. Diko, P.; Pagáčová, R.; Zmorayová, K.; Kuchárová, V.; Vojtková, L.; Antal, V.; Kavečanský, V. Influence of addition of nanosize barium cerate on the microstructure and properties of top-seeded melt growth YBCO bulk superconductors. J Am Ceram Soc 2021, 104, 740-752. http://doi.org/10.1111/jace.17496
53. Kim, C.-J.; Park, H.-W.; Kim, K.-B.; Lee, K.-W.; Gye-Won Hong, G.-W.H. Preparation and critical current density of melt-textured Y-Ba-Cu-O superconductor containing fine Y2BaCuO5 inclusions. Jpn J Appl Phys 1995, 34, L671. http://dx.doi.org/10.1143/JJAP.34.L671
54. Wang, M.; Yang, W.-M.; Li, J.-W.; Feng, Z.-L.; Yang, P.-T. Comparison of the superconducting properties in GdBCO bulk superconductors fabricated with two different solid phases. Supercond Sci Technol 2015, 28, 035004. http://dx.doi.org/10.1088/0953-2048/28/3/035004
55. Wang, M.; Yang, P.-t.; Yang, W.-m.; Li, J.-w.; Hassan, Q.U.I. The fabrication process of a high performance and pure c-axis grown GdBCO bulk superconductor with the TSMT-IG technique. Supercond Sci Technol 2015, 28, 105011. http://dx.doi.org/10.1088/0953-2048/28/10/105011
56. Namburi, D.K.; Shi, Y.; Dennis, A.R.; Durrell, J.H.; Cardwell, D.A. A robust seeding technique for the growth of single grain (RE)BCO and (RE)BCO–Ag bulk superconductors. Supercond Sci Technol 2018, 31, 044003. http://dx.doi.org/10.1088/1361-6668/aaad89
57. Pavel, D. Growth-related microstructure of melt-grown REBa2Cu3Oy bulk superconductors. Supercond Sci Technol 2000, 13, 1202. http://dx.doi.org/10.1088/0953-2048/13/8/317
58. Shen, T.M.; Li, P.; Ye, L.Y. Heat treatment control of Bi-2212 coils: I. Unravelling the complex dependence of the critical current density of Bi-2212 wires on heat treatment. Cryogenics. 2018, 89, 95-101. http://dx.doi.org/10.1016/j.cryogenics.2017.11.006
59. Jiang, J.Y.; Bradford, G.; Hossain, S.I.; Brown, M.D.; Cooper, J.; Miller, E.; Huang, Y.B.; Miao, H.P.; Parrell, J.A.; White, M.; et al. High-performance Bi-2212 round wires made with recent powders. IEEE Trans. Appl. Supercond. 2019, 29, 6400405. http://dx.doi.org/10.1109/tasc.2019.2895197
60. Sager, D.; Meier, L.P.; Gauckler, L.J.; Chen, M. Influence of precursor calcination parameters on the critical current density of Bi-2212 superconductors. Physica C. 2006, 434, 125-134. https://doi.org/10.1016/j.physc.2005.11.017
61. Zhang, Y.; Koch, C.C.; Schwartz, J. Formation of Bi2Sr2CaCu2Ox/Ag multifilamentary metallic precursor powder-in-tube wires. Supercond Sci Technol 2016, 29, 125005. http://doi.org/10.1088/0953-2048/29/12/125005
62. Nane, O.; Özçelik, B.; Amaveda, H.; Sotelo, A.; Madre, M.A. Improvement of structural and superconducting properties of Bi-2212 textured rods by substituting sodium. Ceramurgia Int. 2016, 42, 8473-8477. http://doi.org/10.1016/j.ceramint.2016.02.068

 doi:10.20944/preprints202603.1268.v1

63. Nane, O.; Özçelik, B.; Sotelo, A.; Madre, M.A. Effect of Na substitution on superconducting properties of Bi-2212 ceramics prepared by sinter-forged process. J Eur Ceram Soc 2017, 37, 1007-1012. http://doi.org/10.1016/j.jeurceramsoc.2016.09.035
64. Zhang, S.N.; Ma, X.B.; Cui, L.J.; Huang, Y.J.; Li, C.S.; Feng, J.Q.; Yan, G.; Zhang, P.X. Influences of Na doping on superconducting properties of Bi-2212 high temperature superconductors. Rare Met. Mater. Eng. 2020, 49, 1184-1190.
65. Hiroi, Z.; Chong, I.; Takano, M. Two-phase microstructures generating efficient pinning centers in the heavily Pb-substituted Bi2Sr2CaCu2O8+δ single crystals. J. Solid State Chem. 1998, 138, 98-110. http://doi.org/10.1006/jssc.1998.7758
66. Shin, D.C.; Kang, S.-J.L.; Chung, H.-S. Dendrite formation in the Bi2Sr2CaCu2O8–Ag system: reactions between Ag and oxide melt. Physica C. 2000, 340, 141-148. http://doi.org/10.1016/s0921-4534(00)00841-8
67. Hamid, N.A.; Abd-Shukor, R. Effects of TiO2 addition on the superconducting properties of Bi-Sr-Ca-Cu-O system. J. Mater. Sci. 2000, 35, 2325-2329. http://dx.doi.org/10.1023/A:1004759801684
68. Margulies, L.; Dennis, K.W.; Kramer, M.J.; McCallum, R.W. Effect of P(O2) and Ag content on the decompisition pathway of Bi2Sr2CaCu2Ox. Physica C. 1996, 266, 62-74. https://doi.org/10.1016/0921-4534(96)00289-4
69. Wong-Ng, W.K.; Cook, L.P.; Jiang, F. Melting equilibria of the Bi-Sr-Ca-Cu-O (BSCCO) system in air: The primary crystallization phase field of the 2212 phase and the effect of silver addition. J Am Ceram Soc 1998, 81, 1829-1838. https://doi.org/10.1111/j.1151-2916.1998.tb02554.x
70. Togano, K.; Kumakura, H.; Maeda, H.; Yanagisawa, E.; Takahashi, K. Properties of Pb-doped Bi-Sr-Ca-Cu-O superconductors. Appl Phys Lett 1988, 53, 1329-1331. http://dx.doi.org/10.1063/1.100452
71. Atilla, C.; Ahmet, E.; Bekir, Ö. Superconductivity of Bi1.6Pb0.4Sr2Ca3Cu4O12. Chin. Phys. Lett. 2002, 19, 1863. http://dx.doi.org/10.1088/0256-307X/19/12/337
72. Kumar, J.; Ahluwalia, P.K.; Kishan, H.; Awana, V.P.S. Significant improvement in superconductivity by substituting Pb at Bi-site in Bi2-xPbxSr2CaCu2O8 with x=0.0 to 0.40. J. Supercond. Novel Magn. 2010, 23, 493-499. http://dx.doi.org/10.1007/s10948-009-0622-2
73. Liu, H.; Liu, L.; Zhang, Y.; Yu, H.; Jin, Z. Melting of the 2212 phase in Bi(Pb)SrCaCuO system. J. Mater. Sci. 1999, 34, 6095-6098. http://dx.doi.org/10.1023/A:1004713702798
74. Holesinger, T.G.; Kennison, J.A.; Marken, K.R.; Hanping, M.; Meinesz, M.; Campbell, S. Compositional and microstructural analysis of high Ic and Jc Bi-2212 conductors. IEEE Trans. Appl. Supercond. 2005, 15, 2562-2565. http://dx.doi.org/10.1109/TASC.2005.847652
75. Cabassi, R.; Delmonte, D.; Abbas, M.M.; Abdulridha, A.R.; Gilioli, E. The role of chemical substitutions on Bi-2212 superconductors. Crystals. 2020, 10, 462. http://doi.org/10.3390/cryst10060462
76. Zhang, S.; Li, C.; Hao, Q.; Lu, T.; Zhang, P. Influences of Yb substitution on the intergrain connections and flux pinning properties of Bi-2212 superconductors. Physica C. 2015, 511, 26-32. http://doi.org/10.1016/j.physc.2015.02.004
77. Zhang, S.; Li, C.; Hao, Q.; Ma, X.; Lu, T.; Zhang, P. Optimization of Bi-2212 high temperature superconductors by potassium substitution. Supercond Sci Technol 2015, 28, 045014. http://dx.doi.org/10.1088/0953-2048/28/4/045014
78. Nachtrab, W.T.; Renaud, C.V.; Wong, T.; Liu, X.T.; Shen, T.M.; Trociewitz, U.P.; Schwartz, J. Development of high superconductor fraction Bi2Sr2CaCu2Ox/Ag wire for MRI. IEEE Trans. Appl. Supercond. 2008, 18, 1184-1187. http://dx.doi.org/10.1109/TASC.2008.920630
79. Holesinger, T.G.; Miller, D.J.; Chumbley, L.S. Melt processing of the Bi2Sr2CaCu2Oy superconductor in oxygen and argon atmospheres. IEEE Trans. Appl. Supercond. 1993, 3, 1178-1181. http://dx.doi.org/10.1109/77.233342
80. Marinkovic, B.A.; Xia, S.K.; Serra, E.T.; Rizzo, F. Influence of processing parameters of partial-melting process on phase assemblage, microstructure and superconducting properties of Bi-2212 bulk material. Mater Chem Phys 2005, 91, 301-312. http://doi.org/10.1016/j.matchemphys.2004.11.026
81. Kameneva, M.Y.; Kozeeva, L.P.; Podberezskaya, N.V.; Naumov, D.Y.; Kurat'eva, N.V.; Fedorov, V.E. Composite microstructures in the Bi-Sr-Ca-Cu-O system. Inorg Mater 2007, 43, 845-852. http://dx.doi.org/10.1134/S0020168507080067

 doi:10.20944/preprints202603.1268.v1

82. Imayev, M.F.; Daminov, R.R.; Popov, V.A.; Kaibyshev, O.A. Melting of Bi2Sr2CaCu2O8+x ceramics under uniform compression. Inorg Mater 2005, 41, 537-541. http://dx.doi.org/10.1007/s10789-005-0164-3
83. Hallstedt, B.; Gauckler, L.J. Revision of the thermodynamic descriptions of the Cu–O, Ag–O, Ag–Cu–O, Bi–Sr–O, Bi–Ca–O, Bi–Cu–O, Sr–Cu–O, Ca–Cu–O and Sr–Ca–Cu–O systems. Calphad. 2003, 27, 177-191. http://doi.org/10.1016/s0364-5916(03)00050-6
84. Masi, A.; Alvani, C.; Armenio, A.A.; Augieri, A.; Celentano, G.; De Marzi, G.; Fabbri, F.; Zignani, C.F.; La Barbera, A.; Padella, F.; et al. Fe(Se,Te) system crystallized in molten chlorides flux: The obtained materials and their characterization. J. Cryst. Growth. 2019, 528, 125268. http://dx.doi.org/10.1016/j.jcrysgro.2019.125268
85. Mizuguchi, Y.; Tomioka, F.; Tsuda, S.; Yamaguchi, T.; Takano, Y. Substitution effects on FeSe superconductor. J Phys Soc Jpn 2009, 78, 074712-074712. http://dx.doi.org/10.1143/jpsj.78.074712
86. Tsurkan, V.; Deisenhofer, J.; Günther, A.; Kant, C.; Klemm, M.; von Nidda, H.A.K.; Schrettle, F.; Loidl, A. Physical properties of FeSe0.5Te0.5 single crystals grown under different conditions. Eur. Phys. J. B. 2011, 79, 289-299. http://dx.doi.org/10.1140/epjb/e2010-10473-5
87. Liu, J.X.; Li, C.S.; Zhang, S.N.; Feng, J.Q.; Zhang, P.X.; Zhou, L. Fabrication of Fe1.1Se0.5Te0.5 bulk by a high energy ball milling technique. Solid State Commun 2017, 267, 39-41. http://dx.doi.org/10.1016/j.ssc.2017.09.006
88. Kamihara, Y.; Watanabe, T.; Hirano, M.; Hosono, H. Iron-based layered superconductor La[O1-xFx]FeAs (x=0.05-0.12) with Tc = 26 K. J AM CHEM SOC 2008, 130, 3296-3297. http://dx.doi.org/10.1021/ja800073m
89. Si, Q.; Yu, R.; Abrahams, E. High-temperature superconductivity in iron pnictides and chalcogenides. Nat. Rev. Mater. 2016, 1, 16017. http://dx.doi.org/10.1038/natrevmats.2016.17
90. Guo, Z.; Muraoka, K.; Gao, H.; Shimada, Y.; Harada, T.; Tokuta, S.; Hasegawa, Y.; Yamamoto, A.; Hata, S. Planar defects and strain distributions in polycrystalline BaFe2As2 superconductors synthesized by mechanochemical methods. Acta Mater 2024, 266, 119648. http://doi.org/10.1016/j.actamat.2024.119648
91. Iida, K. Status of iron based superconductors: Characteristics and relevant properties for applications. IEEE Trans. Appl. Supercond. 2025, 35, 1-9. http://dx.doi.org/10.1109/TASC.2025.3530910
92. Liu, G.; Li, J.; Chen, K. Reaction mechanism in fast combustion synthesis of superconducting FeSe and FeSe0.7Te0.3. Acta Mater 2017, 122, 187-198. http://doi.org/10.1016/j.actamat.2016.09.056
93. Zhao, J.; Liao, J.; Dong, C.; Wang, D.; Ma, Y. Properties and applications of iron-chalcogenide superconductors. Materials. 2024, 17, 3059. http://doi.org/10.3390/ma17133059
94. Sylva, G.; Bellingeri, E.; Bernini, C.; Celentano, G.; Ferdeghini, C.; Leveratto, A.; Lisitskiy, M.; Malagoli, A.; Manca, N.; Mancini, A.; et al. The role of texturing and thickness of oxide buffer layers in the superconducting properties of Fe(Se,Te) coated conductors. Supercond Sci Technol 2020, 33, 114002. http://dx.doi.org/10.1088/1361-6668/abb35d
95. Song, J.N.; Xu, Z.T.; Xiong, X.M.; Yuan, W.; Dong, C.H.; Sun, Q.; Tang, M.H.; Chen, W.P.; Tian, H.F.; Li, J.Q.; et al. Critical role played by interface engineering in weakening thickness dependence of superconducting and structural properties of FeSe0.5Te0.5-coated conductors. ACS Appl. Mater. Interfaces. 2023, 15, 26215-26224. http://dx.doi.org/10.1021/acsami.3c04531
96. Fan, F.; Xu, Z.; Cheng, Z.; Huang, H.; Zhu, Y.; Liu, S.; Dong, C.; Zhang, X.; Ma, Y. Enhanced superconducting properties of FeSe0.8Te0.2 thin films grown by pulsed laser deposition. Physica C. 2019, 564, 55-58. http://doi.org/10.1016/j.physc.2019.06.003
97. Yuan, P.; Xu, Z.; Ma, Y.; Sun, Y.; Tamegai, T. Optimization of deposition conditions to grow high-quality Fe-Se-Te thin films. IEEE Trans. Appl. Supercond. 2017, 27, 1-5. http://dx.doi.org/10.1109/TASC.2016.2636570
98. Bhatia, V.; Rodriguez, E.E.; Butch, N.P.; Paglione, J.; Green, M.A. Phase separation and superconductivity in Fe1+xTe0.5Se0.5. Chem. Commun. 2011, 47, 11297-11299. http://dx.doi.org/10.1039/c1cc13878b
99. Sala, A.; Palenzona, A.; Bernini, C.; Caglieris, F.; Cimberle, M.R.; Ferdeghini, C.; Lamura, G.; Martinelli, A.; Pani, M.; Putti, M. The role of Fe deficiency in FeySe0.5Te0.5 samples prepared by a melting process. Physica C. 2013, 494, 69-73. http://doi.org/10.1016/j.physc.2013.05.026
100. Masi, A.; Alvani, C.; Armenio, A.A.; Augieri, A.; Barba, L.; Campi, G.; Celentano, G.; Chita, G.; Fabbri, F.; Zignani, C.F.; et al. Fe(Se,Te) from melting routes: the influence of thermal processing on microstructure

 doi:10.20944/preprints202603.1268.v1

and superconducting properties. Supercond Sci Technol 2020, 33, 084007. http://dx.doi.org/10.1088/1361-6668/ab9acf

101. Masi, A.; Alvani, C.; Augieri, A.; Bellusci, M.; Celentano, G.; Marzi, G.D.; Fabbri, F.; Zignani, C.F.; Barbera, A.L.; Padella, F.; et al. Fe(Se,Te) from melting routes: Insight on phase separation. IEEE Trans. Appl. Supercond. 2019, 29, 1-4. http://dx.doi.org/10.1109/TASC.2019.2899213
102. Yeh, K.-W.; Huang, T.-W.; Huang, Y.-l.; Chen, T.-K.; Hsu, F.-C.; M. Wu, P.; Lee, Y.-C.; Chu, Y.-Y.; Chen, C.-L.; Luo, J.-Y.; et al. Tellurium substitution effect on superconductivity of the α-phase iron selenide. EPL. 2008, 84, 37002. http://dx.doi.org/10.1209/0295-5075/84/37002
103. Palenzona, A.; Sala, A.; Bernini, C.; Braccini, V.; Cimberle, M.R.; Ferdeghini, C.; Lamura, G.; Martinelli, A.; Pallecchi, I.; Romano, G.; et al. A new approach for improving global critical current density in Fe(Se0.5Te0.5) polycrystalline materials. Supercond Sci Technol 2012, 25, 115018. http://dx.doi.org/10.1088/0953-2048/25/11/115018
104. Chen, N.; Liu, Y.; Ma, Z.; Li, H. Significant enhancement of superconducting properties in the FeSe0.5Te0.5 bulks by minor Sn addition. Mater Lett 2016, 175, 16-19. http://doi.org/10.1016/j.matlet.2016.03.137
105. McQueen, T.M.; Huang, Q.; Ksenofontov, V.; Felser, C.; Xu, Q.; Zandbergen, H.; Hor, Y.S.; Allred, J.; Williams, A.J.; Qu, D.; et al. Extreme sensitivity of superconductivity to stoichiometry in Fe1+δSe. Phys. Rev. B. 2009, 79, 014522. http://dx.doi.org/10.1103/PhysRevB.79.014522
106. Terao, K.; Kashiwagi, T.; Shizu, T.; Klemm, R.A.; Kadowaki, K. Superconducting and tetragonal-to-orthorhombic transitions in single crystals of FeSe1-xTex ($0 \le x \le 0.61$). Phys.Rev.B. 2019, 100, 224516. http://dx.doi.org/10.1103/PhysRevB.100.224516
107. Sales, B.C.; Sefat, A.S.; McGuire, M.A.; Jin, R.Y.; Mandrus, D.; Mozharivskyj, Y. Bulk superconductivity at 14 K in single crystals of Fe1+yTexSe1−x. Phys. Rev. B. 2009, 79, 094521. http://dx.doi.org/10.1103/PhysRevB.79.094521
108. Zhang, A.M.; Xia, T.L.; Kong, L.R.; Xiao, J.H.; Zhang, Q.M. Effects on superconductivity of transition-metal doping in FeSe0.5Te0.5. J. Phys.: Condens. Matter. 2010, 22, 245701. http://dx.doi.org/10.1088/0953-8984/22/24/245701
109. Gawryluk, D.J.; Fink-Finowicki, J.; Wiśniewski, A.; Puźniak, R.; Domukhovski, V.; Diduszko, R.; Kozłowski, M.; Berkowski, M. Growth conditions, structure and superconductivity of pure and metal-doped FeTe1−xSex single crystals. Supercond Sci Technol 2011, 24, 065011. http://dx.doi.org/10.1088/0953-2048/24/6/065011
110. Liu, C.Y.; Zhang, H.; Zhao, K.; Cai, F.G.; Yang, X.S.; Zhao, Y. Increased critical current density in iron selenide telluride crystals doping with trace amount of cobalt. J Appl Phys 2025, 137, 073901. http://dx.doi.org/10.1063/5.0252231
111. Liu, J.; Shao, B.; Liu, X.; Li, M.; Sang, L.; Zhang, W.; Zhang, S.; Feng, J.; Li, C.; Dou, S.; et al. Improving superconducting performance of Fe(Se, Te) with in situ formed grain-boundary strengthening and flux pinning centers. ACS Appl. Mater. Interfaces. 2022, 14, 2246-2254. http://dx.doi.org/10.1021/acsami.1c18906
112. Liu, J.X.; Shao, B.T.; Liu, X.Q.; Li, M.; Sang, L.N.; Zhang, W.; Zhang, S.N.; Feng, J.Q.; Li, C.S.; Dou, S.X.; et al. Improving superconducting performance of Fe(Se, Te) with in situ formed grain-boundary strengthening and flux pinning centers. Acs Applied Materials and Interfaces 2022, 14, 2246-2254. http://dx.doi.org/10.1021/acsami.1c18906
113. Galluzzi, A.; Buchkov, K.; Tomov, V.; Nazarova, E.; Kovacheva, D.; Leo, A.; Grimaldi, G.; Pace, S.; Polichetti, M. Mixed state properties of iron based Fe(Se,Te) superconductor fabricated by Bridgman and by self-flux methods. J Appl Phys 2018, 123, 233904. http://dx.doi.org/10.1063/1.5032202
114. Wittlin, A.; Aleshkevych, P.; Przybylińska, H.; Gawryluk, D.J.; Dłużewski, P.; Berkowski, M.; Puźniak, R.; Gutowska, M.U.; Wiśniewski, A. Microstructural magnetic phases in superconducting FeTe0.65Se0.35. Supercond Sci Technol 2012, 25, 065019. http://dx.doi.org/10.1088/0953-2048/25/6/065019
115. Hu, H.; Zuo, J.-M.; Wen, J.; Xu, Z.; Lin, Z.; Li, Q.; Gu, G.; Park, W.K.; Greene, L.H. Phase separation in the iron chalcogenide superconductor Fe1+yTexSe1−x. New J. Phys. 2011, 13, 053031. http://dx.doi.org/10.1088/1367-2630/13/5/053031
116. Miao, C.; Liu, L.; Li, Y. Effect of the cycle number of multistep sintering on the properties of FeSe0.4Te0.6 superconductors. J Am Ceram Soc 2024, 107, 6172-6179. http://doi.org/10.1111/jace.19898

 doi:10.20944/preprints202603.1268.v1

117. Xing, X.; Sun, Y.; Yi, X.; Li, M.; Feng, J.; Meng, Y.; Zhang, Y.; Li, W.; Zhou, N.; He, X.; et al. Electronic transport properties and hydrostatic pressure effect of FeSe0.67Te0.33 single crystals free of phase separation. Supercond Sci Technol 2021, 34, 055006. http://dx.doi.org/10.1088/1361-6668/abef4e
118. Matsumoto, A.; Hatakeyama, H.; Kitaguchi, H.; Togano, K.; Kumakura, H. The superconducting properties of MgB2/(stainless steel) tapes fabricated by the PIT process. IEEE Trans. Appl. Supercond. 2003, 13, 3225-3228. http://dx.doi.org/10.1109/TASC.2003.812206
119. Matsushita, T.; Kiuchi, M.; Yamamoto, A.; Shimoyama, J.; Kishio, K. Critical current density and flux pinning in superconducting MgB2. Physica C. 2008, 468, 1833-1835. http://doi.org/10.1016/j.physc.2008.05.094
120. Yeoh, W.K.; Kim, J.H.; Horvat, J.; Xu, X.; Qin, M.J.; Dou, S.X.; Jiang, C.H.; Nakane, T.; Kumakura, H.; Munroe, P. Control of nano carbon substitution for enhancing the critical current density in MgB2. Supercond Sci Technol 2006, 19, 596. http://dx.doi.org/10.1088/0953-2048/19/6/030
121. Noudem, J.G.; Bernstein, P.; Dupont, L.; Martin, F.G.R.; Sotelo, G.G.; Dias, D.H.N.; de Andrade, R.; Muralidhar, M.; Murakami, M. Spark plasma sintering of bulk MgB2 and levitation force measurements. Supercond Sci Technol 2020, 33, 024001. http://dx.doi.org/10.1088/1361-6668/ab5f3e
122. Muralidhar, M.; Higuchi, M.; Jirsa, M.; Diko, P.; Kokal, I.; Murakami, M. Improved critical current densities of bulk MgB2 using carbon-coated amorphous boron. IEEE Trans. Appl. Supercond. 2017, 27, 1-4. http://dx.doi.org/10.1109/TASC.2016.2637341
123. Liu, M.-X.; Gan, Z.-Z. The upper critical field in two-band layered superconductors. Chin. Phys. 2007, 16, 826. http://dx.doi.org/10.1088/1009-1963/16/3/045
124. Gallitto, A.A.; Bonsignore, G.; Vigni, M.L.; Giunchi, G.; Nefyodov, Y.A. Microwave response of a cylindrical cavity made of bulk MgB2 superconductor. Physica C. 2008, 468, 66-71. http://doi.org/10.1016/j.physc.2007.10.016
125. Iwasa, Y. HTS and NMR/MRI magnets: Unique features, opportunities, and challenges. Physica C. 2006, 445-448, 1088-1094. http://doi.org/10.1016/j.physc.2006.05.040
126. Nagamatsu, J.; Nakagawa, N.; Muranaka, T.; Zenitani, Y.; Akimitsu, J. Superconductivity at 39 K in magnesium diboride. Nature. 2001, 410, 63-64. http://dx.doi.org/10.1038/35065039
127. Matthews, G.A.B.; Santra, S.; Ma, R.; Grovenor, C.R.M.; Grant, P.S.; Speller, S.C. Effect of the sintering temperature on the microstructure and superconducting properties of MgB2 bulks manufactured by the field assisted sintering technique. Supercond Sci Technol 2020, 33, 054003. http://dx.doi.org/10.1088/1361-6668/ab7c53
128. Papagelis, K.; Arvanitidis, J.; Margadonna, S.; Iwasa, Y.; Takenobu, T.; Pissas, M.; Prassides, K. Phase separation in carbon-doped MgB2 studied by means of alternating current susceptibility measurements. J. Phys.: Condens. Matter. 2002, 14, 7363. http://dx.doi.org/10.1088/0953-8984/14/31/307
129. Arvanitidis, J.; Papagelis, K.; Prassides, K.; Kourouklis, G.A.; Ves, S.; Takenobu, T.; Iwasa, Y. Raman spectroscopic study of carbon substitution in MgB2. J. Phys. Chem. Solids. 2004, 65, 73-77. http://doi.org/10.1016/j.jpcs.2003.08.010
130. Hassan, S.S.M.; Fathy, M.A. A novel solid-state iodide ion-selective electrode based on copper-doped MgB2 superconductor. Microchem J 2025, 218, 115639. http://doi.org/10.1016/j.microc.2025.115639
131. Ning, B.Q.; Jiang, H.; Yan, Z.S. Sintering mechanism of Ag-doped MgB2 superconductor from low temperature to high temperature. J Mater Sci - Mater Electron 2010, 21, 666-670. http://dx.doi.org/10.1007/s10854-009-9974-4
132. Shi, Q.Z.; Jiang, H.; Yan, Z.S. Phase formation sequences and mechanism of MgB2 superconductor with minor Sn doping. J Mater Sci - Mater Electron 2010, 21, 1240-1243. http://dx.doi.org/10.1007/s10854-009-0053-7
133. Adriano, C.; Xu, M.; Huyan, S.; Pakuszewski, K.R.; Machado, A.P.; Schrunk, B.; Bud'ko, S.L.; Ribeiro, R.A.; Canfield, P.C.; Kaminski, A. Tuning the electronic properties of MgB2 by substitution with Mn and C. J. Phys.: Condens. Matter. 2025, 37, 305502. http://dx.doi.org/10.1088/1361-648X/adeb27
134. Chen, S.K.; Tan, K.Y.; Tan, K.B.; Shaari, A.H.; Kursumovic, A.; MacManus-Driscoll, J.L. Optimizing C incorporation into magnesium diboride. IEEE Trans. Appl. Supercond. 2011, 21, 2627-2630. http://dx.doi.org/10.1109/TASC.2010.2089420

 doi:10.20944/preprints202603.1268.v1

135. Sumption, M.D.; Bhatia, M.; Dou, S.X.; Rindfliesch, M.; Tomsic, M.; Arda, L.; Ozdemir, M.; Hascicek, Y.; Collings, E.W. Irreversibility field and flux pinning in MgB2 with and without SiC additions. Supercond Sci Technol 2004, 17, 1180. http://dx.doi.org/10.1088/0953-2048/17/10/017
136. Yamamoto, A.; Shimoyama, J.; Ueda, S.; Katsura, Y.; Horii, S.; Kishio, K. Doping effects on critical current properties of MgB2 bulks synthesized by modified powder-in-tube method. IEEE Trans. Appl. Supercond. 2005, 15, 3292-3295. http://dx.doi.org/10.1109/TASC.2005.848855
137. Zhao, Y.; Feng, Y.; Cheng, C.H.; Zhou, L.; Wu, Y.; Machi, T.; Fudamoto, Y.; Koshizuka, N.; Murakami, M. High critical current density of MgB2 bulk superconductor doped with Ti and sintered at ambient pressure. Appl Phys Lett 2001, 79, 1154-1156. http://dx.doi.org/10.1063/1.1396629
138. Wang, J.; Bugoslavsky, Y.; Berenov, A.; Cowey, L.; Caplin, A.D.; Cohen, L.F.; MacManus Driscoll, J.L.; Cooley, L.D.; Song, X.; Larbalestier, D.C. High critical current density and improved irreversibility field in bulk MgB2 made by a scaleable, nanoparticle addition route. Appl Phys Lett 2002, 81, 2026-2028. http://dx.doi.org/10.1063/1.1506184
139. Gao, Z.; Santra, S.; Amirkhanlou, S.; Eardley, E.; Wort, C.; Grovenor, C.R.M.; Speller, S.C. Microstructures and superconducting properties of MgB2 bulk samples processed by ultra-high pressure-assisted sintering. J Eur Ceram Soc 2022, 42, 7481-7490. http://doi.org/10.1016/j.jeurceramsoc.2022.09.008
140. Huang, Z.; Cai, X.; Xi, D.; Luo, W.; Guo, C.; Feng, Q.; Nie, R.; Wang, F.; Gan, Z. Low-temperature sintering to fabricate MgB2 by using Mg(BH4)2 as precursor. Supercond Sci Technol 2021, 34, 075007. http://dx.doi.org/10.1088/1361-6668/abff70
141. Sklyarova, A.; Presmanes, L.; Baylac, V.; Chevallier, G.; Estournès, C.; Duployer, B.; Noudem, J.; Bernstein, P.; Tailhades, P.; Thimont, Y. Processing of bulk MgB2 superconductors by coupling laser powder bed fusion and spark plasma sintering techniques. Materials. 2025, 18, 2367. http://doi.org/10.3390/ma18102367
142. Shimada, Y.; Hata, S.; Ikeda, K.-i.; Nakashima, H.; Matsumura, S.; Tanaka, H.; Yamamoto, A.; Shimoyama, J.-i.; Kishio, K. Microstructural connectivity in sintered ex-situ MgB2 bulk superconductors. J Alloys Compd 2016, 656, 172-180. https://doi.org/10.1016/j.jallcom.2015.09.253
143. Birajdar, B.; Eibl, O.; Braccini, V.; Grasso, G.; Pachla, W.; Herrman, M.; Häßler, W. Correlation of superconducting properties and microstructure of MgB2 wires and tapes. Physica C. 2007, 460-462, 1409-1410. https://doi.org/10.1016/j.physc.2007.04.121
144. Matsumoto, A.; Hatakeyama, H.; Kitaguchi, H.; Togano, K.; Kumakura, H. The superconducting properties of MgB2 (stainless steel) tapes fabricated by the PIT process. IEEE Trans. Appl. Supercond. 2003, 13, 3225-3228. http://dx.doi.org/10.1109/TASC.2003.812206
145. Matthews, G.A.B.; Mousavi, T.; Santra, S.; Grovenor, C.R.M.; Grant, P.S.; Speller, S. Improving the connectivity of MgB2 bulk superconductors by a novel liquid phase sintering process. Supercond Sci Technol 2022, 35, 065005. http://dx.doi.org/10.1088/1361-6668/ac5164